

The locations of halo formation and the peaks formalism

Oliver Hahn^{*1} and Aseem Paranjape^{†1}

¹*Institute for Astronomy, Department of Physics, ETH Zurich, CH-8093 Zürich, Switzerland*

MNRAS in press

ABSTRACT

We investigate the problem of predicting the halo mass function from the properties of the Lagrangian density field. We focus on a perturbation spectrum with a small-scale cut-off (as in warm dark matter cosmologies). This cut-off results in a strong suppression of low mass objects, providing additional leverage to rigorously test which perturbations collapse and to what mass. We find that all haloes are consistent with forming near peaks of the initial density field, with a strong correlation between proto-halo density and ellipticity. We demonstrate that, while standard excursion set theory with correlated steps completely fails to reproduce the mass function, the inclusion of the peaks constraint leads to the correct number of haloes but significantly underpredicts the masses of low-mass objects (with the predicted halo mass function at low masses behaving like $dn/d \ln m \sim m^{2/3}$). This prediction is very robust and cannot be easily altered within the framework of a single collapse barrier. The nature of collapse in the presence of a small-scale cut-off thus reveals that excursion set calculations require a more detailed understanding of the collapse-time of a general ellipsoidal perturbation to predict the ultimate collapsed mass of a peak – a problem that has been hidden in the large abundance of small-scale structure in CDM. We demonstrate how this problem can be resolved within the excursion set framework.

Key words: cosmology: theory, dark matter, large-scale structure of Universe – galaxies: formation – methods: N-body, numerical, analytical

1 INTRODUCTION

Where and when do dark matter haloes form? The problem of identifying the locations where gravitational collapse leads to bound haloes of dark matter, and predicting the cosmic time at which this will occur, is among the oldest problems of cosmic structure formation theory. The idea that small perturbations in the primordial matter density formed the seeds of the large-scale structure we observe at present is among the cornerstones of our current picture of the evolution of the Universe. An understanding of the relevant processes and a robust theoretical model enables us to map properties such as the abundance and clustering of dark matter haloes – which are directly tied to the corresponding observed properties of galaxies – to well-understood statistical properties of the *initial* dark matter density.

Although this problem can now be tackled directly using numerical simulations of large, cosmological volumes, it is still important to explore analytical approximations and identify the key physical features that decide the sites of halo formation. The main motivation behind this exercise is to gain a better understanding of the physical processes that affect structure formation in the Universe. From a practical viewpoint, however, this can also lead to useful, fast approximations to the halo

mass function, clustering, and predictions of collapse time for a given patch in the initial conditions. The latter especially could be useful from the point of view of “semi-analytic” mock catalog algorithms such as PTHALOS (Scoccimarro & Sheth 2002), PINOCCHIO (Monaco et al. 2002, 2013), COLA (Tassev, Zaldarriaga, & Eisenstein 2013), ALPT (Kitaura & Heß 2013), etc., which are becoming increasingly popular in the construction of covariance matrices in current and upcoming surveys such as BOSS (Manera et al. 2013), WiggleZ (Marín et al. 2013), Euclid (Laureijs et al. 2011), and others.

Our focus in this paper is on the mass function of dark matter haloes, which is the most basic diagnostic of the fully non-linear density field. Analytical descriptions of the halo mass function have traditionally used two parallel approaches: the excursion set approach (Press & Schechter 1974; Epstein 1983; Peacock & Heavens 1990; Bond et al. 1991; Lacey & Cole 1993; Sheth 1998; Sheth et al. 2001; Maggiore & Riotto 2010; Paranjape et al. 2012; Musso & Sheth 2012; Achitouv et al. 2012; Musso & Sheth 2013) and the peaks formalism (Bardeen et al. 1986; Bond 1989; Appel & Jones 1990; Manrique et al. 1998; Hanami 2001), both of which aim to characterize the locations of collapse in the initial conditions using some criteria. The former relies on counting sufficiently overdense regions in the initial conditions, which it maps to collapsed haloes in the final, gravitationally evolved density field, while the latter associates haloes specifically to peaks in the initial matter density. In other words, while both approaches rely on

* Email:hahn@phys.ethz.ch

† Email:aseemp@phys.ethz.ch

the statistical properties of the initial conditions to predict final halo abundances, the excursion set approach does this by treating all locations in the initial conditions on the same footing, while the peaks formalism treats density peaks as being special.

The key aspect of the excursion set approach (Bond et al. 1991), which is missing in the traditional peaks approach (Bardeen et al. 1986), is that it explicitly accounts for the so-called “cloud-in-cloud” problem which avoids overcounting overdense regions embedded in larger overdense regions as individual objects. The “peak-patch” approach of Bond & Myers (1996) is a numerical prescription for unifying the two approaches to solve the cloud-in-cloud problem for peaks, or, equivalently, to study excursion sets for a special subset of initial locations, namely peaks. Recent work (Musso & Sheth 2012; Paranjape & Sheth 2012) has shown that this can also be achieved analytically by making some simple but accurate approximations (see also Bond 1989). There are several motivations for doing so (Sheth, Mo, & Tormen 2001; Paranjape & Sheth 2012), not least the fact that N -body simulations of cold dark matter (CDM) show that a large fraction of haloes do, in fact, originate from initial density peaks (Ludlow & Porciani 2011b). Further, Paranjape, Sheth, & Desjacques (2013) showed that this unified analytical formalism of excursion set peaks (ESP) gives a self-consistent description of the CDM halo mass function as well as clustering which is accurate at the $\sim 10\%$ level.

It is worth asking whether this formalism has correctly captured all the relevant aspects of structure formation that affect the mass function. One way of addressing this issue is to apply the same formalism in an “extreme” situation which it was not explicitly built to describe. Structure formation from an initial matter power spectrum with highly suppressed small-scale power, as found in warm dark matter (WDM) cosmologies, offers the perfect playground. The reason is that, apart from having a truncated initial power spectrum, *simulations of WDM in fact solve exactly the same problem as those of CDM*: the evolution of a cold, collisionless, self-gravitating fluid.

Analytically, one then expects that the same ESP expressions, which correctly describe the CDM mass function and clustering, should work for the WDM case as well, with the simple replacement of the CDM initial power spectrum with that of WDM. In this regard, as we describe in detail below, the “out-of-the-box” ESP calculation does considerably better than traditional TopHat-filtered excursion sets: it correctly predicts a turnover in $dn/d\ln m$ at the correct scale whereas the latter predicts a monotonic rise at low masses. We will see, however, that ESP predicts a power law decrease at low masses $dn/d\ln m \sim m^{2/3}$ which is incompatible with the results of simulations. This analytical prediction is very robust and hints at a missing physical ingredient in the excursion set logic¹.

¹ We should note that previous authors (e.g., Benson et al. 2013; Schneider et al. 2013) have motivated a standard excursion set analysis of the WDM mass function (without the peaks constraint) by appealing to a smoothing filter that is sharp in Fourier space. While the resulting mass function fits are straightforward to implement, the physical relevance of the sharp- k filter is less clear. Although there might be a deeper reason behind its success (e.g., it could be that the real-space nonlocality inherent in the sharp- k filter somehow captures the properties of the initial density environment near small mass WDM peaks better than, say, the TopHat filter), we believe it is important to first assess how well the physically motivated picture

Our goal in this paper is to characterise the collapsed objects identified in a WDM simulation in terms of the properties of the initial density field. This will allow us to understand the reasons behind the mismatch of the measured mass function and the ESP prediction. The paper is structured as follows:

In Section 2, we describe the numerical simulation and halo finding algorithm, which are the same as presented by Angulo, Hahn, & Abel (2013). We then compare the resulting halo mass function with theoretical expectations based on the ESP formalism, and discuss possible reasons for the differences we see between the theory and numerics. To better understand where haloes form, in Sections 3 and 4 we turn to an in-depth analysis of the initial conditions of the simulation. In Section 3 we analyse the initial density field at the “Lagrangian patches” of the haloes (i.e., the initial locations of groups of particles that will eventually be identified as haloes) and demonstrate that all haloes in the simulation are consistent with forming near peaks of the initial density. We also explore correlations between the initial overdensity and shape of the Lagrangian patches, and use these results to motivate the construction of an empirical catalogue of “ESPeaks”, which we describe in Section 4. These ESpEaks are a numerical realisation of what the ESP calculation aims to accomplish, and we compare their Lagrangian properties with those of the haloes.

Our main conclusion from this exercise is that, while the ESP calculation on average correctly identifies the locations of halo formation, it systematically underpredicts the mass of the resulting object, and that this effect is especially enhanced at halo masses that are small compared to the characteristic mass scale where the WDM mass function turns around. In Section 5 we argue that this mass mismatch is related to a systematic overprediction of the *time* of collapse of a given perturbation, and propose a modification to the ESP calculation to re-assign masses by correcting for this effect. We show that the resulting mass function not only agrees very well with the WDM result, but also describes the CDM mass function accurately with the simple replacement of the WDM power spectrum with that of CDM.

We close with a summary and discussion in Section 6. The Appendices collect technical details and arguments used to motivate some of the results in the main text.

2 THE HALO MASS FUNCTION: CONFRONTING SIMULATIONS AND THEORY

Matter power spectra with an initial small-scale truncation arise naturally in warm and hot dark matter cosmologies where density fluctuations on small scales are suppressed due to the late transition to the non-relativistic regime of the respective dark matter particle. Such a power spectrum leads to a corresponding turn-over in the late time halo mass function. The numerical determination of such mass functions has, however, proven extremely challenging due to the presence of low mass objects that arise – completely unphysically – from the fragmentation of filaments (see e.g. Avila-Reese et al. 2001; Bode et al. 2001; Wang & White 2007; Melott 2007; Hahn et al. 2013). In the presence of artificial fragmentation, mass functions can only be measured indirectly after filtering or correcting for

of peaks itself fares. We will therefore not pursue sharp- k filtering in this paper.

the spurious haloes (see e.g. Lovell et al. 2012; Schneider et al. 2012; Lovell et al. 2013). Only more recently has the behaviour of the halo mass function around and below the turn-over scale been explicitly demonstrated by Angulo et al. (2013, AHA13, in what follows).

While such WDM cosmologies are of course of genuine physical interest in their own right, we are mainly concerned with a different aspect here: the suppression of *low* mass haloes provides powerful additional leverage to test models of structure formation in such cosmologies. The exponential fall in the halo mass function at large masses – whose sensitivity to cosmological parameters has been exploited for decades – is replicated here at the small-mass end. Any theoretical model must now describe both of these strong features in the mass function.

We begin by briefly discussing the numerical simulations of AHA13 and the WDM halo mass function they measure. We will see that these numerical results do not meet theoretical expectations based on the ESP formalism. We discuss possible reasons for this, which will motivate our subsequent analysis.

2.1 Numerical Simulation

The numerical simulation discussed by AHA13 employs the novel T4PM method (Hahn et al. 2013), which completely suppresses artificial fragmentation and allows the determination of the halo mass function at and below the turn-over scale in the absence of numerical artefacts.

Specifically, this simulation resolves a $80 h^{-1}\text{Mpc}$ cosmological volume with 1024^3 particles with cosmological parameters $\Omega_m = 0.276$, $\Omega_\Lambda = 0.724$, $\Omega_b = 0.045$, $h = 0.703$, $\sigma_8 = 0.811$ and $n_s = 0.96$, consistent with the WMAP7 data release (Komatsu et al. 2011). The normalisation of the power spectrum using σ_8 was set using a CDM spectrum, so that the amplitude of fluctuations on large-scales is independent of the truncation scale of the power spectrum.

The truncation of power at small scales is done by assuming a toy model cosmology with a 0.25 keV thermally produced WDM particle. Such a particle is, of course, completely ruled out by observations as the dominant component of dark matter (see e.g. Viel et al. 2013, who derive a current lower bound of 3.3 keV). However, it allows resolving the entire power spectrum up to the truncation scale with sufficient particles and, as we have already argued above, is studied in this paper for the main purpose of testing analytical predictions. In particular, AHA13 used the fitting formula of Bode et al. (2001) to modify the CDM transfer function

$$T_{\text{WDM}}(k) = T_{\text{CDM}}(k) [1 + (\alpha k)^2]^{-5.0}, \quad (1)$$

with

$$\alpha \equiv 0.05 \left(\frac{\Omega_m}{0.4}\right)^{0.15} \left(\frac{h}{0.65}\right)^{1.3} \left(\frac{m_{\text{dm}}}{1\text{ keV}}\right)^{-1.15} h^{-1}\text{Mpc}, \quad (2)$$

where $m_{\text{dm}} (= 0.25\text{ keV})$ is the DM particle mass. This results in $\alpha = 0.26 h^{-1}\text{Mpc}$, equivalent to a free-streaming mass-scale

$$M_{\text{fs}} = \frac{4\pi}{3} \bar{\rho} (\alpha/2)^3 \simeq 7 \times 10^8 h^{-1} M_\odot, \quad (3)$$

and a “half-mode” mass-scale (c.f., e.g., Schneider et al. 2012)

$$M_{\text{hm}} \simeq 4.3 \times 10^3 M_{\text{fs}} \simeq 3.0 \times 10^{12} h^{-1} M_\odot. \quad (4)$$

Note that, as discussed in more detail in AHA13, these simulations do not include the (small) thermal velocity dispersion that a real WDM fluid would possess, so that the collisionless

dark matter fluid is in fact treated in the perfectly cold limit, after perturbations have been suppressed below the maximum free-streaming scale in linear perturbation theory. A thermal velocity however is expected to have little effect on the abundance of collapsed structures at late times, which is the main topic of our interest here.

Adopting the fit of Eisenstein & Hu (1999) as the fiducial CDM transfer function T_{CDM} , initial conditions were generated using the MUSIC code (Hahn & Abel 2011) at an initial redshift of $z = 63$ using the Zel’dovich approximation. We note that a simulation initialized at such a rather low redshift using first order Lagrangian perturbation theory is to some degree affected by transients from the initial conditions (e.g. Crocce et al. 2006). The high-mass end of the halo mass function is thus expected to deviate from the true one. The small volume of the simulation adds further to a systematic deviation. Furthermore, it is possible that the detailed behaviour of the mass function around the half-mode mass is also affected by transients. This possibility needs to be considered for precision determinations of the halo mass function but we do not expect it to alter the qualitative behaviour with which we are mostly concerned here (the results of AHA13 are roughly consistent with, e.g., the predictions of Schneider et al. 2013 who use 2LPT). We note that the half-mode mass is resolved with almost $100'000$ particles in the simulation of AHA13.

2.2 Halo Identification

AHA13 found that the suppression of artificial fragmentation leads to a failure of the Friends-of-Friends (FoF) halo finder. The dense cores of filaments (in the absence of artificial fragmentation) lead to a percolation of large regions of several haloes when the standard linking parameter $b = 0.2$ is used. Instead, they first adopted a linking parameter of $b = 0.05$ times the mean inter-particle separation and then determined the spherical-overdensity (SO) mass centred on the centre-of-mass of the parent FoF group. A halo was defined as the sphere of radius R_{200} , which has a mean density of 200 times the critical density, ρ_{crit} . This corresponds to a halo mass $M_{200} = (4\pi/3) R_{200}^3 (200\rho_{\text{crit}})$.

Further, by analyzing all haloes individually, AHA13 found that the halo sample could be divided into various subsamples or “types”. “Type-1” objects are virialized haloes, while “type-2” include haloes in late stages of formation; the latter do not show an isotropic density structure and instead contain larger scale caustics that are remnants of their formation. The remaining objects were haloes in early stages of formation, that have, e.g., just started collapsing along the third axis.

In what follows, we only consider the “type-1” objects clearly identified as haloes. The red histogram in Figure 1 is identical to the line labelled “haloes” in Figure 7 of AHA13 and shows the mass function of these “type-1” haloes, which has a sharp cut-off between 10^{11} - $10^{12} h^{-1} M_\odot$. (The other two histograms will be discussed in Section 4 below.) It is important to note here that the classification was performed visually and we thus expect that, on an object-by-object basis, the distinction between type 1 and 2 is likely not perfectly robust.

2.3 Theoretical expectations

As discussed earlier, as far as late time structure formation is concerned, the only difference between the CDM and WDM cosmologies is the lack of *initial* small scale power in the latter.

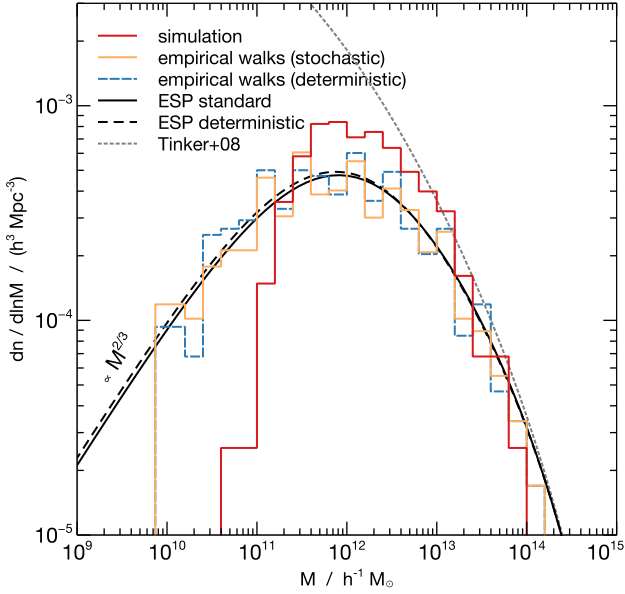


Figure 1. Halo mass functions: the abundance of virialized objects in the simulation (red) as well as the mass functions of “ESPeaks” determined using empirical excursion set walk starting at peak locations from the same initial conditions as the simulation using the barrier in equation (28) (orange; see Section 4.1 for details). The dashed blue histogram shows the result of the same algorithm but now using the deterministic barrier $B = \delta_c + 0.5\sigma_0$. The solid black line shows the “standard” analytic ESP calculation from Paranjape et al. (2013) which used a stochastic barrier adjusted to match CDM simulations. The dashed black line shows the ESP calculation using the deterministic barrier mentioned above (see Section 5 for details). Although peaks theory correctly predicts a turn-over in the mass function at the correct scale, it gets the asymptotic behaviour below this scale wrong. For comparison, the dotted black line shows the result of using the Tinker et al. (2008) fitting formula.

So one might expect that a physically motivated description of CDM structure should apply equally well to WDM – at least at scales much larger than the free-streaming scale – with the simple replacement of the CDM transfer function with the one in equation (1). One can already anticipate that the standard hierarchical excursion set calculation would have difficulty in describing the low mass end of the WDM mass function where the effective logarithmic slope of the power spectrum $n_{\text{eff}} \equiv d \ln P(k) / d \ln k$ becomes steeper than -3 . This is the boundary beyond which hierarchical prescriptions are known to fail, with predicted mass accretion rates becoming ill-defined (Lacey & Cole 1993, 1994). The ESP formalism, however, introduces a new ingredient into the picture – the peaks constraint – and since we know that it works well for CDM, we can ask what it predicts for the WDM case.

In what follows, we will frequently use integrals over the power spectrum of the filtered initial overdensity field δ_R and its spatial derivatives, all linearly extrapolated to the present epoch:

$$\sigma_j^2(R) \equiv \int d \ln k \Delta(k) k^{2j} \tilde{W}_R(k)^2, \quad (5)$$

where $\Delta(k) \equiv k^3 P(k, z=0) / (2\pi^2)$ is the dimensionless matter power spectrum in linear theory and $\tilde{W}_R(k)$ is the Fourier transform of the smoothing filter, for which we will use a spherical TopHat $\tilde{W}_R(k) = 3(\sin kR - kR \cos kR) / (kR)^3$ in our numer-

ical analysis and later also a Gaussian $\tilde{W}_R(k) = \exp(-k^2 R^2 / 2)$ in our analytical modelling². The above definitions correspond to setting $\sigma_0^2(R) = \langle \delta_R^2 \rangle$, $\sigma_1^2(R) = \langle (\nabla \delta_R)^2 \rangle$ and $\sigma_2^2(R) = \langle (\nabla^2 \delta_R)^2 \rangle$ and appear in peaks formalism calculations. Another quantity, which is relevant for excursion set models of the mass function, is the derivative of the smoothed density field with respect to smoothing scale, $d\delta_R/dR$, which is in general different from the spatial derivatives of δ_R . A special case is that of Gaussian filtering, for which $d\delta_R/dR = R \nabla^2 \delta_R$, a result which will be useful later in our analytical modelling. For TopHat filtering, $d\delta_R/dR$ and $\nabla^2 \delta_R$, although different, are strongly correlated (Paranjape et al. 2013).

To get an idea about the scale of the problem, consider that simply counting all peaks in the unsmoothed initial density field of the WDM simulation gives us 6713 objects, where “unsmoothed” refers to the density on a 512^3 grid and a grid cell is labelled a peak if its density is higher than all its 26 neighbours (see Section 3 for more details). This grid size just about resolves the cutoff scale α (equation 2) below which no initial fluctuations exist; we have verified that a 1024^3 grid (the resolution at which the initial conditions of AHA13 were generated) leads to a consistent result (6822 peaks). This matches very well with the theoretical prediction for this number in the simulation volume V_{box} (equation 4.11b of Bardeen et al. 1986, BBKS from here on):

$$N_{\text{pk}} = n_{\text{pk}} V_{\text{box}} = 3.12 \times 10^{-3} (\sigma_2 / \sigma_1)^3 V_{\text{box}} = 6608,$$

in which we evaluated σ_1 and σ_2 using equation (5) with $R = 0$ and the transfer function (1). Comparing this with the number of “type-1” objects in the simulation – 1522 – we clearly see that not every individual peak forms a halo. This is fully expected within the analytical framework – e.g., there is nothing special about a peak of height $\delta = -10\sigma_0$ – and we will show later that the ESP calculation does lead to a number close to the measured number of haloes.

The ESP halo mass function can be written as (Paranjape & Sheth 2012; Paranjape et al. 2013)

$$dn_{\text{ESP}} / d \ln m = \mathcal{N}_{\text{ESP}} |d\nu / d \ln m|, \quad (6)$$

where $\nu \equiv \delta_c(z) / \sigma_0(m)$ with $\delta_c(z)$ being the critical linear overdensity or “barrier” for spherical collapse in a Λ CDM background³, and where \mathcal{N}_{ESP} has the structure

$$\mathcal{N}_{\text{ESP}} \sim \frac{1}{V_*} \times g_{\text{ESP}}(\nu, \gamma). \quad (7)$$

Here $g_{\text{ESP}}(\nu, \gamma)$ is a dimensionless function of its arguments (details in Section 5), and γ and V_* are spectral quantities that define the distribution of peaks (BBKS):

$$\gamma \equiv \sigma_1^2 / (\sigma_0 \sigma_2) \quad ; \quad V_* \equiv (6\pi)^{3/2} (\sigma_1 / \sigma_2)^3. \quad (8)$$

² All these integrals remain finite at all scales, including the unsmoothed limit $R \rightarrow 0$, since the WDM free-streaming scale itself acts as a smoothing filter. In contrast, ultraviolet power in CDM causes $\sigma_0(R)$ and $\sigma_1(R)$ to diverge as $R \rightarrow 0$, while the TopHat smoothed $\sigma_2(R)$ always diverges, meaning that any analysis of small scale CDM peaks would be limited by effects at the spatial resolution limit of the simulation.

³ The redshift dependence of $\delta_c(z)$ in a flat Λ CDM universe is slightly different from that in an Einstein-deSitter background (see, e.g., Eke et al. 1996), and can be approximated by $\delta_{c,\text{EoS}}(z) D(z) / D(0) = \delta_{c,\text{EoS}}(1 - 0.0123 \log_{10}(1 + x^3))$, where $x \equiv (\Omega_m^{-1} - 1)^{1/3} / (1 + z)$ and $\delta_{c,\text{EoS}} = 1.686$ (Henry 2000). In our case, requiring collapse at present epoch gives $\delta_c(z=0) = 1.674$.

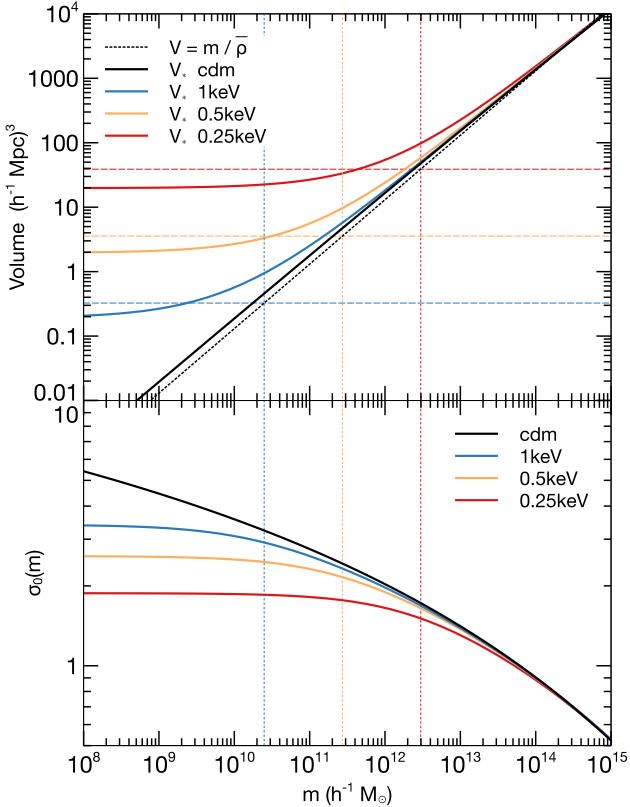


Figure 2. (*Top panel:*) Characteristic peak volume V_* (solid curves) defined in equation (8), for CDM (black) and three choices of WDM particle mass m_{dm} ; from bottom to top: 1keV (blue), 0.5keV (yellow), 0.25keV (red). Dotted black line shows the Lagrangian volume $V = m/\bar{\rho}$. For CDM, V_* closely tracks V . For WDM, as m decreases, V_* tracks V until $m \sim M_{\text{hm}}$ (vertical dotted lines) and then approaches a constant value close to $M_{\text{hm}}/\bar{\rho}$ (horizontal dashed lines). All the V_* curves used Gaussian filtering as described in Appendix A. (*Bottom panel:*) The relation between σ_0 and mass m with TopHat filtering for CDM (black) and when using equation (1) with the same particle masses (and colour-coding) as in the top panel. For WDM we clearly see a “freezing-out” of $\sigma_0(m)$ at small masses.

Whereas γ is a dimensionless measure of the width of the power spectrum, V_* sets the mean number density of all peaks on scale R (equation 4.11b of BBKS).

It is easy to see that the spectral integrals σ_j , and consequently also ν , γ and V_* , will each approach a constant value for WDM as $m \rightarrow 0$. The behaviour of ν and V_* in this respect is very different from that in CDM in the same limit, where $\nu, V_* \rightarrow 0$ as $m \rightarrow 0$. This reflects the fact that peaks can only form on scales large enough to be inhomogeneous; *reducing the smoothing scale cannot wipe out existing peaks for any power spectrum and, for a truncated spectrum, cannot introduce new peaks*. This can be seen in the top panel of Figure 2: for each choice of m_{dm} , V_* at large m is close to the CDM value (and hence approximately proportional to $V = m/\bar{\rho}$, where $\bar{\rho}$ is the comoving mean density), but deviates as m approaches the half-mode mass M_{hm} , finally approaching a constant value at $m \ll M_{\text{hm}}$, this value being close to $M_{\text{hm}}/\bar{\rho}$. This last aspect gives us an interesting physical interpretation of the half-mode mass as being essentially the same as the asymptotic peaks scale.

Finally, the Jacobian appearing in equation (6) behaves,

as $m \rightarrow 0$ for WDM, like

$$\left| \frac{d\nu}{d \ln m} \right| = \frac{\nu^3 R}{3\delta_c(z)^2} \int d \ln k \Delta(k) W(kR) \left| \frac{dW}{dR} \right| \rightarrow \frac{R^2 \nu^3}{\#\delta_c(z)^2} \int d \ln k \Delta(k) k^2 \propto R^2 \propto m^{2/3}, \quad (9)$$

where $\# = 15$ for a TopHat filter and 3 for a Gaussian filter, so that the ESP mass function (equation 6) for WDM at small masses behaves like

$$dn_{\text{ESP}}/d \ln m \sim |d\nu/d \ln m| \sim m^{2/3}. \quad (10)$$

This power-law behaviour at small masses will be true for any single-barrier excursion set model of peaks in which the barrier depends on halo mass only through the spectral integrals; in particular, this behaviour is independent of details such as barrier shape, stochasticity, etc.

The behaviour of V_* discussed above shows that the turnover occurs at around $m \sim M_{\text{hm}}$. The solid curve in Figure 1 shows the ESP calculation of Paranjape et al. (2013) using the WDM transfer function (1). The dashed curve shows the ESP result with a somewhat different, convenient choice of barrier for the random walks, which we will discuss in detail in Section 5.2 below. The main point is that both of these curves show the turnover and the asymptotic scaling of $\sim m^{2/3}$. As discussed above, the latter is a very robust prediction that cannot be easily altered by technical modifications within the framework of a single barrier.

It is interesting to contrast this result with the corresponding one for the traditional excursion set approach, as this emphasizes the key role played by the behaviour of V_* . For traditional excursion sets (Bond et al. 1991; Musso & Sheth 2012), one has

$$dn_{\text{trad}}/d \ln m = (\bar{\rho}/m) f(\nu) |d\nu/d \ln m|. \quad (11)$$

where $f(\nu)$ is a dimensionless function analogous to $g_{\text{ESP}}(\nu, \gamma)$ discussed earlier. More importantly, V_* is replaced by the Lagrangian volume $V = m/\bar{\rho}$ of the halo, so that for WDM at small masses, this mass function behaves like

$$dn_{\text{trad}}/d \ln m \sim m^{-1} |d\nu/d \ln m| \sim m^{-1/3}. \quad (12)$$

This asymptotic behaviour is unphysical because the hierarchical excursion set calculation should not predict objects at small masses where no hierarchical formation can occur in the absence of small scale power (See the discussion above equation 5). The dotted curve in Figure 1 shows the result of using equation (1) to compute the relation $\sigma_0(m)$ in the CDM fit provided by Tinker et al. (2008). For completeness, the bottom panel of Figure 2 compares the $\sigma_0(m)$ relation for TopHat filtering when using equation (1) with the corresponding relation for CDM. For WDM we clearly see a “freezing-out” of $\sigma_0(m)$ at small masses. The other spectral integrals also show similar behaviour.

2.4 Theory vs. Simulation – What could be going wrong?

Although the physical requirement of being a density peak naturally accounts for a turnover in the mass function at the correct mass scale, the asymptotic scaling (very robustly) predicted by ESP is clearly wrong. There are several issues which could in principle affect this result:

Dynamics: A dramatic possibility is that, since small-mass

haloes in WDM do not form hierarchically (e.g., at some point in time the first object forms, with no virialized progenitor), the peaks calculation might simply not be applicable. This would lead to the interesting question of just what it is that characterizes the locations and dynamics of the collapse of small mass objects. The cut-off scale in the initial spectrum could in principle allow for higher order catastrophes (c.f. Arnold et al. 1982) to become relevant, and these need not necessarily appear as peaks when filtered on the proto-halo scale. In CDM, the situation is quite different in this respect, since fluctuations persist down to very small scales and so every proto-halo has a progenitor at a smaller scale.

Barrier shape: It has been argued that the collapse barrier appropriate for WDM haloes is very different from the corresponding CDM one due to thermal effects in WDM, and that this can introduce a sharp cut-off in the mass function (Benson et al. 2013). However, since WDM simulations see a cut-off despite ignoring thermal effects (e.g., AHA13; Schneider et al. 2013), the origin of the cut-off must be rooted in the suppression of *initial* small scale power, and must therefore be a generic feature of cold collisionless dynamics in such conditions. The failure of excursion set (peaks) models to reproduce the correct mass function hence indicates quite clearly that these models are still not accounting for some important physical processes. One of the primary goals of this work is to investigate the cause of this behaviour.

Patch shape: Traditional excursion sets, as well as the ESP calculation of Paranjape et al. (2013), use spherical filters when assigning masses to objects, and it could be that asphericity of the Lagrangian patches affects the mass assignment significantly at small masses. E.g., recently Despali, Tormen, & Sheth (2013) have demonstrated using CDM simulations that accounting for halo asphericity using an ellipsoidal halo finder can lead to small increases in mass for low mass haloes (see also Ludlow & Porciani 2011a).

Stochasticity: Regardless of the importance of thermal effects, the specific details of the barrier, e.g., those related to stochasticity in the barrier height, are in fact somewhat uncertain (even in the CDM case). The ESP calculation for CDM is self-consistent but not fully predictive, and needs some inputs from simulations (Paranjape et al. 2013). In particular, the barrier used in that calculation was adjusted to match measurements by Robertson et al. (2009) of proto-halo overdensity in CDM simulations, and the same results might not apply in the case of WDM.

Peak-in-peak: Another possible source of error is that the ESP framework treats the peak-in-peak problem approximately, by introducing the effects of the peaks constraint as an extra weight in the mass function, rather than by explicitly accounting for spatial correlations between walks centred at different locations in space (see, e.g., Scannapieco & Barkana 2002), and this approximation needs testing.

We address these issues in the next two Sections by exploring the properties of the initial conditions of the simulation in greater detail⁴.

⁴ A further role might be played by assembly bias, i.e., the dependence of halo formation histories on scales substantially larger than the Lagrangian patch. Assembly bias is typically seen as a suppression of late-time growth for low-significance haloes (c.f., e.g., Sheth & Tormen 2004; Gao et al. 2005; Desjacques 2008; Hahn et al. 2009; Fakhouri & Ma 2010). The impact of large-scale tidal fields on the collapse of scales around the half-mode scale, where

3 LAGRANGIAN PROPERTIES OF HALOES

In this Section, we turn to the initial conditions of the simulation and perform an in-depth study of the Lagrangian properties of regions that will eventually form haloes; we call such regions proto-haloes and give a precise definition below. Several authors have performed such studies in CDM simulations (e.g., White 1996; Bond & Myers 1996; Sheth et al. 2001; Porciani et al. 2002; Robertson et al. 2009; Ludlow & Porciani 2011a,b; Elia et al. 2012; Despali et al. 2013). To our knowledge, the current work is the first to extend these studies to the case of WDM, and is interesting for the reasons discussed in Section 2.

An advantage of using a WDM model with $m_{\text{dm}} = 0.25\text{keV}$ is that the number of objects is reasonably small. A disadvantage is that the half-mode mass is close to being unit-significance, $\nu(M_{\text{hm}}, z=0) \simeq 0.9$, which does not allow us to explore low-significance objects with sufficient statistical precision. This could also potentially confuse non-linear assembly-bias-like effects with the peculiarities of halo formation at and below the half-mode mass scale. Nevertheless, this simulation provides us with an invaluable testing ground for several ideas in the peaks framework.

We focus on the overdensity of the proto-halo patch (which is indicative of the collapse threshold), its curvature, velocity shear (ellipticity and prolateness) and moment of inertia. We will demonstrate two important features of the proto-halo patches; (a) that they are all consistent with forming at initial density peaks and (b) their overdensities are strongly correlated with their ellipticities but not their prolateness.

3.1 Lagrangian density and shear fields

The initial conditions code MUSIC allows us to output the density field that was used to generate the simulation initial conditions as three-dimensional grid data. We used this function to re-generate the density field directly on a 512^3 mesh with the same Fourier modes as the original simulation. We refer to this as the unsmoothed field δ . Using the particle IDs that encode the three dimensional Lagrangian coordinate \mathbf{q} on the unperturbed initial particle lattice (i.e. before applying the Zel'dovich approximation), we can directly evaluate the density at \mathbf{q} without interpolating the perturbed particle position back on a grid. We linearly scale the density field to $z=0$.

Using the unsmoothed density field on a mesh, we compute various derived fields using the fast Fourier transform (FFT). We compute the gradient and the Hessian of the density field,

$$\nabla\delta = \mathcal{F}^{-1} \left\{ i\mathbf{k}\tilde{\delta}(\mathbf{k}) \right\}, \quad \partial_{ij}\delta = \mathcal{F}^{-1} \left\{ -k_i k_j \tilde{\delta}(\mathbf{k}) \right\}, \quad (13)$$

where the tilde indicates the Fourier transformed field. Additionally, we compute the velocity potential as well as its Hessian (the so-called tidal tensor which reflects the velocity shear),

$$\psi = \mathcal{F}^{-1} \left\{ -k^{-2}\tilde{\delta}(\mathbf{k}) \right\}, \quad \partial_{ij}\psi = \mathcal{F}^{-1} \left\{ \frac{k_i k_j}{k^2} \tilde{\delta}(\mathbf{k}) \right\}, \quad (14)$$

so that the velocity field is $\mathbf{u} \propto -\nabla\psi$. When computing filtered fields, we replace $\tilde{\delta}(\mathbf{k})$ with $\tilde{\delta}_R(\mathbf{k}) = \tilde{\delta}(\mathbf{k})\tilde{W}_R(k)$.

We define the ordered eigenvalues of $\partial_{ij}\delta$ as $\zeta_1 \leq \zeta_2 \leq \zeta_3$ and those of the velocity shear $\partial_{ij}\psi$ as $\lambda_1 \leq \lambda_2 \leq \lambda_3$. The

structure formation is not hierarchical, has (to our knowledge) not been studied yet. This aspect would clearly be of interest in future work.

normalised negative trace of the density Hessian gives us the dimensionless peak curvature

$$x \equiv -(\zeta_1 + \zeta_2 + \zeta_3)/\sigma_2, \quad (15)$$

while the trace of the velocity shear gives back the density

$$\delta = \text{Tr } \partial_{ij}\psi = \lambda_1 + \lambda_2 + \lambda_3 \propto -\text{div } \mathbf{u}. \quad (16)$$

Peaks in δ are thus equivalent to regions of maximum convergence in the Lagrangian flow. We will also need the ellipticity e_v and prolateness p_v associated with the tidal tensor:

$$e_v \delta \equiv (\lambda_3 - \lambda_1)/2 \equiv Y, \quad (17)$$

$$p_v \delta \equiv (\lambda_3 - 2\lambda_2 + \lambda_1)/2 \equiv Z, \quad (18)$$

where we have defined Y and Z to be the corresponding unnormalised quantities which will be useful below. Similarly, we can define

$$e_{\text{pk}} x \equiv -(\zeta_1 - \zeta_3)/(2\sigma_2) \equiv y, \quad (19)$$

$$p_{\text{pk}} x \equiv -(\zeta_1 - 2\zeta_2 + \zeta_3)/(2\sigma_2) \equiv z, \quad (20)$$

so that e_{pk} and p_{pk} describe the shape of the peak (BBKS).

3.2 Proto-haloes and their properties

For each halo, we recorded the particle IDs and recovered their respective Lagrange coordinates \mathbf{q} . We call the set of N_k Lagrangian particles comprising halo k its Lagrangian patch or proto-halo, denoted $L_k \equiv \{\mathbf{q}_i \mid i = 1 \dots N_k\}$.

We compute the patch average of a Lagrangian field $f(\mathbf{q})$ by evaluating

$$\langle f \rangle_k^{(\text{p})} = \frac{1}{N_k} \sum_{\mathbf{q}_i \in L_k} f(\mathbf{q}_i). \quad (21)$$

and the spherical average by first determining the Lagrange radius $R_L = (3m/4\pi\bar{\rho})^{1/3}$, where m is the halo mass, and then evaluating

$$\langle f \rangle_k^{(\text{s})} = (f \otimes W_{R_L})(\mathbf{q}_{\text{med}}). \quad (22)$$

Here W_{R_L} is the TopHat filter at scale R_L and \mathbf{q}_{med} is the median Lagrange coordinate of the Lagrangian patch, where the median is taken of each separate Cartesian component. Using the median instead of the mean coordinate reduces the influence of outliers in the Lagrangian patch.

Figure 3 shows three examples of proto-haloes with masses $\sim 10^{13} h^{-1} M_\odot$. The top panel shows a well behaved proto-halo. We notice two disconnected shells surrounding the connected interior of this patch. This is a beautiful example of the mapping between Lagrangian and Eulerian space. The gaps between the shells appear because the outer caustics of the halo are not inside the virial radius and are thus cut off. The two shells correspond to material on first and second infall. The other two examples show evidence of mixing due to large scale interactions.

In addition to the ellipticity and prolateness associated with the density Hessian, we can also characterize the shape of the Lagrangian patch L_k through the dimensionless reduced moment of inertia tensor

$$I_{ij} = \sum_{\mathbf{q} \in L_k} (\mathbf{q}^2 \delta_{ij} - q_i q_j) / \mathbf{q}^2, \quad (23)$$

which we define to be centred on the centre-of-mass of the object (rather than its median location), since this minimises its values.

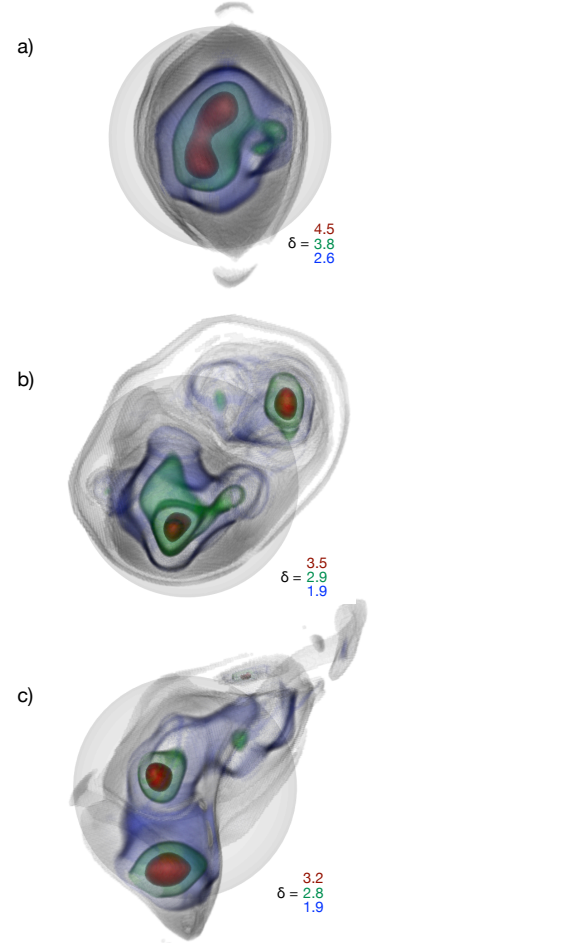


Figure 3. Volume renderings of the (unsmoothed) density field in the proto-halo patches for three haloes of mass $10^{13} h^{-1} M_\odot$. Each panel shows a light grey sphere centred on the proto-halo centre, containing the same mass. The darker shaded gray volume indicates the actual proto halo patch. Coloured contours indicate isodensity regions at the values given underneath each image. (*Top panel:*) A good example of an ellipsoidal proto-halo patch, with clearly visible disconnected outer regions. This proto-halo was also assigned a matching ESPeak by the algorithm described in Section 4. (*Middle & bottom panels:*) Two examples of proto-haloes with evidence for substantial substructure and mixing due to large scale interactions. Our algorithm did not find any matching ESPeak for these two objects.

The eigenvalues $\iota_1 \leq \iota_2 \leq \iota_3$ of I_{ij} give the corresponding axes of the homogeneous ellipsoid $a \leq b \leq c$:

$$\begin{aligned} a &= \sqrt{5/2N_k} (\iota_1 + \iota_2 - \iota_3), \\ b &= \sqrt{5/2N_k} (\iota_1 - \iota_2 + \iota_3), \\ c &= \sqrt{5/2N_k} (-\iota_1 + \iota_2 + \iota_3), \end{aligned} \quad (24)$$

and the sphericity

$$S \equiv a/c. \quad (25)$$

3.3 Haloes form at peaks

We start by verifying statistically that haloes in cosmologies with truncated small-scale power do indeed form from peaks. Being a peak requires the overdensity field δ to be locally

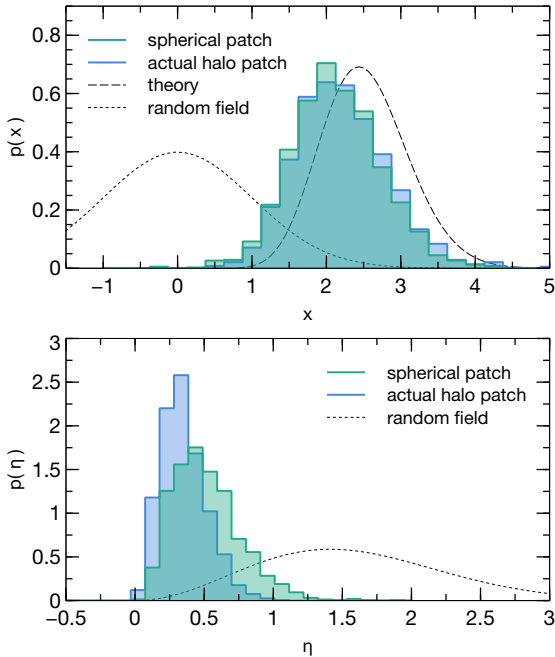


Figure 4. (*Top panel:*) The distribution of peak curvatures x (equation 15) at proto-halo locations, averaged over the Lagrangian patch (blue histogram) and using a spherical aperture of the same mass (green histogram). The dashed curve shows the theoretically expected distribution (equation 36) while the dotted curve shows the distribution at random locations (a Gaussian with zero mean and unit variance). (*Bottom panel:*) The distribution of density gradient $\eta \equiv \sqrt{3}|\nabla\delta|/\sigma_1$ at proto-halo locations, averaged over the Lagrangian patch (blue histogram) and using a spherical aperture of the same mass (green histogram). The dotted line is the distribution at random locations; in this case η^2 is distributed as Chi-squared with 3 degrees of freedom. These plots show that all haloes in our sample are consistent with having formed near initial density peaks.

extremal on the scale of the proto-halo, i.e.

$$\langle \nabla\delta \rangle = \mathbf{0} \quad \text{and} \quad \langle \zeta_i \rangle < 0, \quad i = 1, 2, 3, \quad (26)$$

We find that all proto-halo patches have $\langle \zeta_i \rangle^{(s)} < 0$ and $\langle \zeta_i \rangle^{(p)} < 0$ and thus the total peak curvature x is positive in both cases. Note that to define averaged eigenvalues of a tensor, we diagonalise after computing the average of the tensor.

In Figure 4, we show the distribution of the total curvature x (equation 15; top panel) and the magnitude of the gradient $\eta \equiv \sqrt{3}|\nabla\delta|/\sigma_1$ (bottom panel) averaged over the halo patches. For computing σ_1 and σ_2 which make these quantities dimensionless, we used a TopHat filter at the Lagrangian scale R_L of each object.

The distribution of x for a Gaussian random field would be a Gaussian with zero mean and unit variance (dotted black curve in the top panel). The measured distribution on the other hand has only positive values as mentioned above, and its shape is very similar to the analytical prediction using ESP with a deterministic barrier (dashed black curve, see Section 5, equation 36), although the measured mean value for x is lower than the predicted mean by about 0.4.

The distribution of η for a Gaussian random field would be $p(\eta) = \sqrt{2/\pi}\eta^2 e^{-\eta^2/2}$ (because in this case η^2 is Chi-squared distributed with 3 degrees of freedom.) This is shown as the dotted black curve in the bottom panel; the measured values

clearly populate the low tail of this distribution. (Ideally all the values would be zero.) We also see that the patch-averaged values of η have a significantly lower scatter than the spherically averaged ones. This is not surprising since the requirement $\eta = 0$ is quite unstable to choices of filtering, and the spherical filter is known to introduce an additional randomisation as compared with the actual Lagrangian patch (BBKS; Despali et al. 2013).

We therefore conclude that all haloes in our sample are consistent with having formed near initial density peaks. In principle, we should also have explicitly checked for the presence of local density maxima at or near the proto-halo locations, e.g., along the lines discussed by Ludlow & Porciani (2011b). This, however, would involve making a specific choice regarding the smoothing scale. We defer such a calculation to Section 4.1, where we implement an algorithm that makes this choice while simultaneously centering the smoothing filter at locations that are most likely to collapse according to the excursion set formalism.

3.4 Overdensity of Lagrangian patches

Figure 5 shows the patch-averaged (left panel) and spherically averaged (middle panel) overdensities of the proto-haloes as a function of their mass. We find that the spherical overdensities are strongly correlated with the corresponding spherically averaged values of Y (equation 17). This is evident in the middle panel where we have coloured the points using $\langle Y \rangle^{(s)}$. (The patch-averaged overdensities show a similar strong correlation with the patch-averaged Y ; we omitted the colouring in the left panel for clarity.)

The right panel of the Figure shows the difference $\langle \delta \rangle^{(s)} - \langle Y \rangle^{(s)}$ coloured by prolateness $\langle Z \rangle^{(s)}$ (equation 18). We see that the scatter in this difference is significantly smaller than that in $\langle \delta \rangle^{(s)}$, and its distribution is curiously similar to that of $\langle \delta \rangle^{(p)}$ with a mean close to the standard spherical collapse value δ_c (horizontal dashed line in all panels). More importantly, we have found no correlation of $\langle \delta \rangle^{(s)}$ with prolateness $\langle Z \rangle^{(s)}$. In other words, the spherical overdensities of the proto-haloes are well approximated by the relation

$$\langle \delta \rangle^s = \delta_c + \langle Y \rangle^s, \quad (27)$$

with a residual scatter that does not correlate with prolateness. This is consistent with the CDM results of Ludlow & Porciani (2011a). We have also checked that the overdensity does not correlate with the other shape parameters y and z defined in equations (19) and (20).

Robertson et al. (2009) performed similar spherically averaged measurements in the initial conditions of the CDM simulations presented by Tinker et al. (2008). The left panel of Figure 5 shows the mean and standard deviation of the distribution of overdensities reported by Robertson et al. (2009), but using the WDM transfer function. We see that their spherically averaged measurements, extrapolated to WDM, are in reasonable agreement with our patch-averaged overdensities. Our spherical overdensities, on the other hand, have a higher mean and scatter than theirs (see also Elia et al. 2012, who found similar results in their CDM simulations). There is no clear reason for this discrepancy.

These results for the spherically averaged overdensity and shear ellipticity will form the basis of the empirical walks that we describe in the next Section. In general, however, we note that our measurements of spherically averaged quantities tend

to have larger scatter than the corresponding patch-averaged ones. For completeness, in Appendix C we also show the distributions of ellipticity and prolateness defined using the tidal tensor and the Hessian of the density.

In summary, the results of this section show us that haloes form at peaks and have Lagrangian (spherically averaged) overdensities that are consistent with equation (27), with a residual scatter that is uncorrelated with other properties such as shear prolateness or peak shapes. One aspect we have not explored here is the relative (mis-)alignment between the velocity shear, density Hessian and moment of inertia tensors, which can be an important ingredient in any recipe for predicting collapse-time based on dynamical arguments. This is especially interesting given previous results from CDM simulations (Porciani et al. 2002; Despali et al. 2013) which suggest that, contrary to expectations based on Gaussian statistics (e.g., van de Weygaert & Bertschinger 1996), the direction of maximum initial compression is on average well-aligned with the longest geometrical axis of the proto-halo, rather than the shortest. We will return to an analysis of tensor alignments and their dynamical consequences in future work.

4 EMPIRICAL EXCURSION SET PEAK WALKS

The most serious issue raised in Section 2.4 was whether or not the excursion set formalism can capture *at all* the formation of haloes in WDM, which does not proceed hierarchically below the half-mode mass scale. In excursion set language, this amounts to asking whether or not the relation

$$B = \delta_c + Y \quad (28)$$

actually works as a barrier for random walks of the density centred on peaks, and whether the resulting objects predicted to collapse from peaks at specific locations with a certain mass bear any relation to the haloes found in the simulation.

To test this, in this Section, we explicitly perform such random walks in the actual initial density field that was used for the numerical simulation and identify spherical peak-patches which are predicted to form haloes using this barrier. We will refer to these objects as ESPEaks below.

Note that the relation (28) is similar to that predicted by the dynamics of a collapsing homogenous ellipsoid, which is well-approximated by (Sheth et al. 2001)

$$B_{ec} = \delta_c \left(1 + \beta_{ec} [5(Y^2 \pm Z^2)/\delta_c^2]^{1/\gamma_{ec}} \right), \quad (29)$$

where $\beta_{ec} = 0.47$ and $\gamma_{ec} = 0.615$ and the minus (plus) sign is to be used when Z is positive (negative). The most important difference is the absence of the prolateness in equation (28). We will return to this issue below.

4.1 Methodology

Our algorithm is essentially a more accurate version of what the analytical ESP calculation tries to achieve. We note that it is less sophisticated than the original peak-patch algorithm implemented by Bond & Myers (1996), since we are not interested in the final locations, profiles and velocity dispersions of the haloes, but only in their mass.

We consider a hierarchy of $N_s = 100$ smoothing scales R_i logarithmically spaced in the TopHat spherical mass contained in R_i between $M_0 = 10^{10} h^{-1} M_\odot$ and $M_{N_s} = 10^{15} h^{-1} M_\odot$. We then proceed as follows, starting with the largest smoothing scale:

1. We determine the coordinates \mathbf{x}_k of all peaks in δ_{R_i} . Being a peak requires that δ_{R_i} is larger at \mathbf{x}_k than in all 26 surrounding cells.
2. We discard all peaks for which δ_{R_i} is below the barrier, i.e. where $\delta_{R_i}(\mathbf{x}_k) < B(\mathbf{x}_k; R_i)$; B is given by equation (28).
3. Additionally, we discard all peaks that are within the Lagrangian radius of a peak that has been identified before. This explicitly solves the cloud-in-cloud problem.
4. Finally, we also discard all peaks where the density was above threshold on a larger scale, i.e. where $\delta_{R_{i+1}}(\mathbf{x}_k) > B(\mathbf{x}_k; R_i)$. This step improves numerical stability but is otherwise redundant.
5. We proceed to the next smaller scale $i \rightarrow i - 1$ and start over at step 1.

A small fraction of objects have partially overlapping Lagrangian volumes. We flag the smaller of such pairs as “sub-peaks” and, for the current analysis, do not include them in the sample of proto-haloes. (These form about 10% of the total sample.) At the end, we arrive at a catalogue of ESPEaks whose Lagrangian properties we can analyse in exactly the same way as for the actual proto-halo patches.

4.2 The mass function of ESPEaks

The solid orange histogram in Figure 1 corresponds to the mass function of ESPEaks obtained using the algorithm described above. The dashed blue histogram shows the result of the same algorithm, but now using a *deterministic* barrier equation (33) which, as we argue in the next section, is a useful approximation to equation (28). Indeed, we see that these two histograms agree quite well, indicating that stochasticity in the barrier arising from statistical fluctuations in the initial conditions does not lead to dramatic effects in the mass function.

The most important feature of the orange histograms is that they show a low mass tail consistent with $dn/d \ln m \propto m^{2/3}$ as discussed earlier. In fact, the histograms are well described by the WDM version of the ESP calculation (solid black) of Paranjape et al. (2013) who used a stochastic barrier adjusted to match CDM simulations, as well as a similar ESP calculation with the deterministic barrier (33) which we discuss below.

The overall number of ESPEaks identified by our algorithm (1261 when using equation 28 and 1335 when using equation 33) is reasonably close to the total number of proto-haloes, which is 1522. The lower numbers of ESPEaks could partially be because we stop our algorithm at the lower mass limit of $10^{10} h^{-1} M_\odot$. For comparison, integrating the ESP prediction using equation (33) (dashed line in Figure 1) above the free-streaming scale M_{fs} gives a prediction of 1380 objects in the simulation volume.

4.3 Matching ESPEaks and haloes

If the excursion set picture is valid, the ESPEaks we identify should be correlated with the actual proto-haloes. Could the mass function mis-match simply be because our low mass ESPEaks are not associated with proto-haloes? To assess this, we match the proto-halo catalogue and the ESPEaks catalogue as follows.

For every proto-halo, we find the ESPEaks contained inside of a sphere of its Lagrangian radius, and associate the ESPEak of highest mass with the halo. This procedure matches 978 (i.e., 64%) of the proto-haloes to ESPEaks. We then repeat the

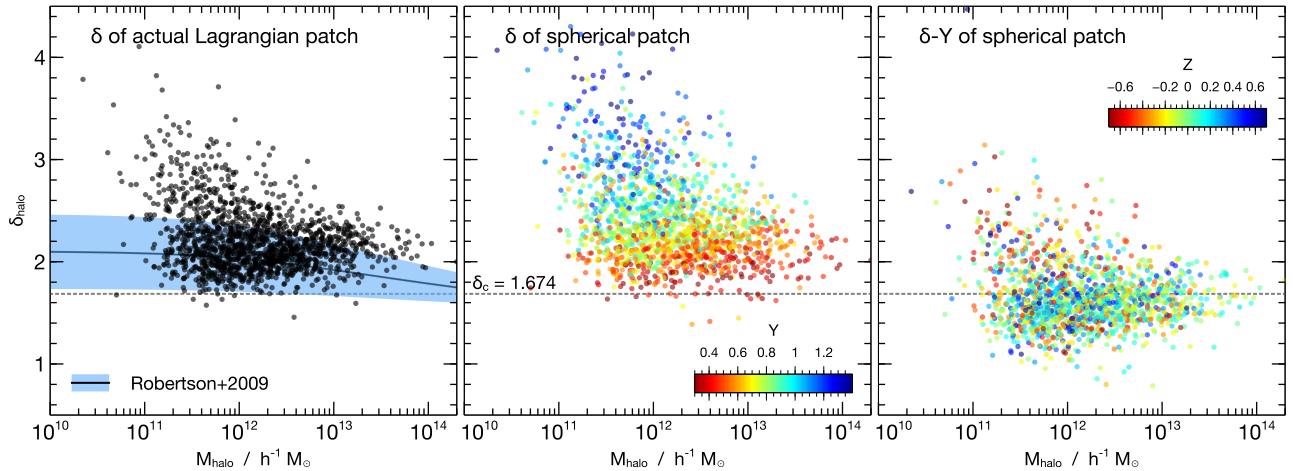


Figure 5. Patch overdensity as a function of proto-halo mass. (*Left panel:*) The overdensity δ (equation 16) at proto-halo locations, averaged over the Lagrangian patch (points). The thick blue line and the blue band show, respectively, the mean and standard deviation of the spherically averaged proto-halo overdensities measured by Robertson et al. (2009) in CDM simulations, extrapolated to our WDM initial power spectrum (i.e., we used our WDM transfer function in the fit in their equation D2 with the $\Delta = 200$ parameters from their Table 1). (*Middle panel:*) Proto-halo overdensity δ averaged over spherical apertures of the same mass, coloured by the spherically averaged ellipticity $Y = e_v \delta$ (equation 17). We see a strong trend of δ with Y , as expected from ellipsoidal collapse arguments (Sheth et al. 2001). (*Right panel:*) The quantity $\delta - Y$, coloured by the spherically averaged prolateness $Z = p_v \delta$ (equation 18). The residual scatter shows no trend with Z , which is at odds with the predictions of ellipsoidal collapse models.

same procedure matching ESPEaks to haloes using the filter radius on which the ESPEak was identified, and in this case we can match 935 (i.e., 74%) of the ESPEaks to proto-haloes. (Including the sub-peaks in the analysis makes these numbers 68% and 72%, respectively.) We discuss possible reasons for the relatively large fraction of mismatched objects below (see also Ludlow & Porciani 2011b). In Appendix C, we also discuss the effect of repeating the exercise with the ellipsoidal collapse barrier (29).

As a visual example, we note that the well-behaved proto-halo in the top panel in Figure 3 was assigned a matching ESPEak while the other two distorted objects were not. While the majority of the proto-haloes we can match to ESPEaks look like the object in the top panel and the majority of unmatched proto-haloes are distorted, there are also a number of examples of well-behaved proto-haloes that are not matched, as well as distorted proto-haloes that are.

The top panel of Figure 6 shows the masses of the proto-haloes that we could match to ESPEaks compared to the corresponding ESPEak masses. The points are coloured by the spherically averaged proto-halo sphericity S (equation 25). There is a strong trend of S with halo mass: low mass haloes are decidedly aspherical. This is consistent with the CDM results of Ludlow & Porciani (2011a). Additionally, the scatter in mass assignment also correlates strongly with S , with low mass, aspherical haloes having the largest scatter. However, at a given halo mass, the mass mismatch *on average* does not seem to correlate strongly with halo shape.

The histograms in the bottom panel of the Figure show the mass function of matched (orange) and unmatched (blue) proto-haloes, with the gray histogram showing the total halo mass function (same as the red histogram in Figure 1). The matched fraction is quite large at the highest masses (reaching 100% for $m \gtrsim 3 \times 10^{13} h^{-1} M_\odot$), remains approximately constant at intermediate masses $m \sim M_{\text{hm}}$ and falls significantly at low masses $m \lesssim 10^{12} h^{-1} M_\odot$.

In the top panel of Figure 7, we show the ratio of ESPEak mass to proto-halo mass as a function of ESPEak mass, for ESPEaks that we could match to haloes, coloured in this case by the spherically averaged proto-halo curvature x . We see a weak trend of curvature with mass mismatch: ESPEaks matching shallower proto-haloes appear to have larger mass mismatches.

The histograms in the bottom panel of the Figure show the mass function of matched (orange) and unmatched (blue) ESPEaks, while the gray histogram is the same as in Figure 6 and shows the mass function of all haloes. We clearly see that most of the unmatched ESPEaks were assigned dramatically lower masses than any proto-halo in the sample. This could indicate that the ESP picture is, in fact, not appropriate for these objects. However, the presence of a small fraction of low mass ESPEaks that *do* have matching proto-haloes, which in turn have *larger* true masses and low curvatures, suggests that the explanation of this trend could be more subtle. We therefore explore the properties of the mismatched objects in more detail in the next subsection. Recall that the sum of the mass functions of matched and unmatched ESPEaks is consistent with analytical ESP predictions (compare the smooth black curves and solid orange histogram in Figure 1).

4.4 Failures of the proto-halo \leftrightarrow ESPEak matching

We have already seen above that the masses of the ESPEaks that cannot be matched to proto-haloes are too low compared to the mass function of haloes. As illustrated in Figure 8, these unmatched proto-haloes tend to have significantly lower peak curvatures and higher densities (solid blue curves in the top and bottom panels, respectively) than those that could be matched to ESPEaks (solid orange curves in the respective panels). Similar trends are also seen, albeit to a lesser extent, in the densities and curvatures of ESPEaks that (do not) have matching proto-haloes, as seen in the dashed orange (blue) curves in the two panels. The inset in the top panel of the

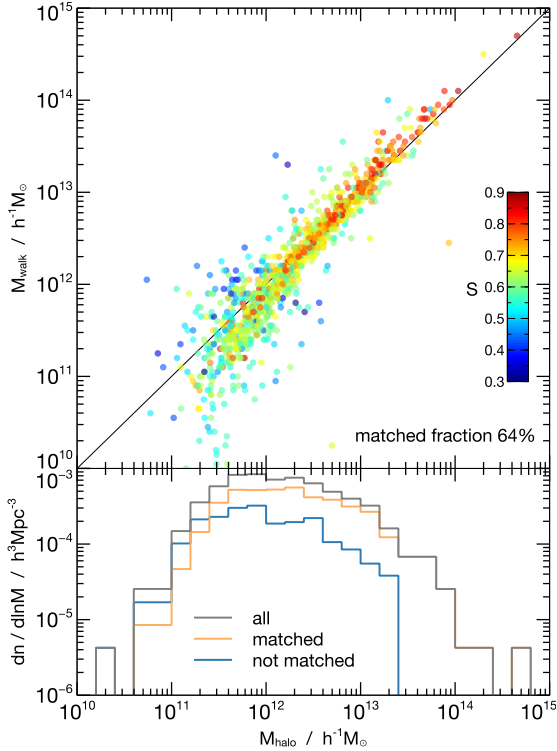


Figure 6. (*Top panel:*) The masses M_{halo} of proto-halos that could be matched to ESpeaks, compared to the corresponding ESpeak mass M_{walk} , coloured by the spherically averaged proto-halo sphericity S (equation 25). Low mass proto-halos are clearly more aspherical than high mass ones, and the scatter in mass assignment also increases significantly for the more aspherical objects. At a given halo mass, however, the average mass mismatch does not correlate strongly with S . (*Bottom panel:*) The orange (blue) histogram shows the mass function of proto-halos that could (not) be matched to ESpeaks. The gray histogram shows the total halo mass function (same as the red histogram in Figure 1). The matched fraction is quite large at high masses and falls significantly at low masses.

Figure shows the joint distribution of curvature and mass for the matched (orange) and mismatched (blue) proto-halos. The absence of a significant mass dependence of x indicates that the difference in peak curvature is not a result of the two populations occupying different mass ranges.

Figure 9 shows the distribution of mass and sphericity S for the matched (orange) and unmatched (blue) proto-halos. There is a strong trend of sphericity with mass, as noted in Figure 6. Apart from this, however, there is no significant difference between the sphericities of matched and unmatched proto-halos. The dashed line, which is somewhat shallower than the measured mass trend, shows the linear fit to corresponding measurements in CDM simulations presented by Ludlow & Porciani (2011a).

4.5 Discussion

Our comparison of the outcomes of simulation and the empirical walks suggests that, at least at masses $m \gtrsim M_{\text{hm}}$, the empirical approach more or less correctly predicts both the locations and masses of collapsed haloes. At smaller masses, however, the algorithm is able to predict the location of a collapsed object only for a relatively small fraction ($\sim 55\%$ of proto-halos below $10^{12} h^{-1} M_{\odot}$ have an associated ESpeak, and the

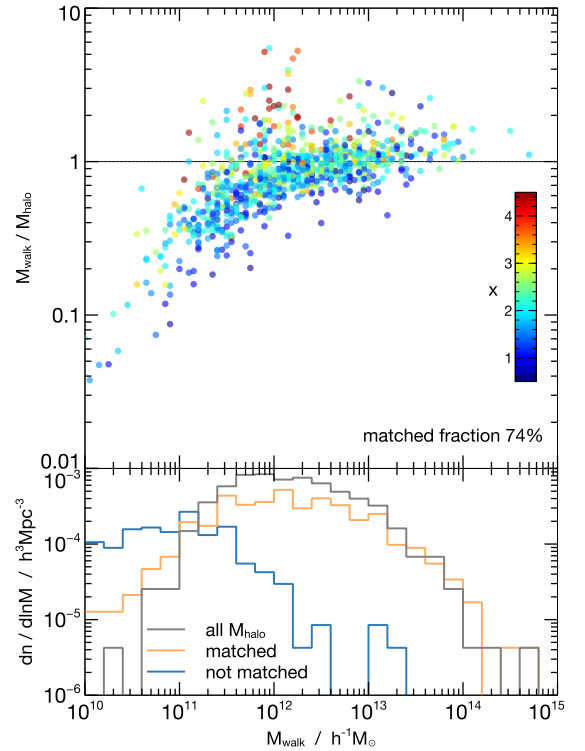


Figure 7. (*Top panel:*) The masses M_{walks} of ESpeaks that could be matched to proto-halos, compared to the corresponding proto-halo mass M_{halo} , coloured by the spherically averaged proto-halo curvature x (equation 15). We see a weak trend of the mass mismatch with curvature: shallower proto-halos tend to have larger mismatches between M_{halo} and M_{walk} . (*Bottom panel:*) The orange (blue) histogram shows the mass function of ESpeaks that could (not) be matched to proto-halos. The gray histogram shows the total halo mass function (same as the red histogram in Figure 1). Most of the unmatched ESpeaks were assigned dramatically lower masses than any proto-halo in the sample. The sum of the orange and blue histograms is consistent with analytical ESP predictions (compare the smooth black curves and solid orange histogram in Figure 1).

fraction falls below 50% quickly below this mass scale) and almost always predicts too small a mass in these cases. The large fraction of ESpeaks that cannot be matched to proto-halos are also predicted to have dramatically lower masses than any proto-halo in the simulation.

We have also seen that, on average, the mass and position mis-matches seem to be uncorrelated with the shapes of the proto-halos. That is to say, although smaller proto-halos are decidedly aspherical (with a scatter in mass mismatch that correlates with sphericity), there seems to be no trend between the average sphericity and the ratio $m_{\text{ESpeak}}/m_{\text{halo}}$ in the matched cases (Figure 6) and no significant difference between sphericities of matched and unmatched proto-halos with $m_{\text{halo}} < M_{\text{hm}}$ (Figure 9).

The unmatched proto-halos do have smaller curvatures than the matched ones. In principle, this could simply be because of their lower masses. However, the absence of a significant mass dependence of x in the inset in the top panel of Figure 8 indicates that this is not the case. Additionally, in the case of ESpeaks matched to proto-halos, the proto-halo curvature correlates with the mass mismatch (Figure 7).

Note that the objects identified in the simulation of AHA13

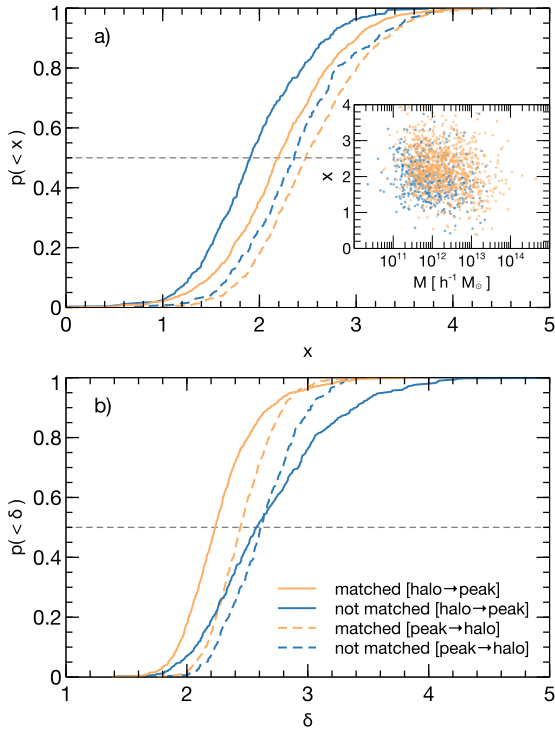


Figure 8. Cumulative distributions of spherically averaged peak curvature (top) and density (bottom) for the proto-haloes that could be matched to ESPEaks (solid orange) and for proto-haloes for which no corresponding ESPEak could be found (solid blue). The dashed orange (blue) curves show the corresponding quantities for ESPEaks that could (not) be matched to proto-haloes. The inset in the top panel shows the joint distribution of proto-halo mass and curvature in the matched (orange) and unmatched (blue) cases. The absence of a significant mass dependence of x shows that the trend seen in the cumulative distribution – unmatched objects have smaller curvatures – is not entirely caused by the preferentially low masses of the unmatched objects.

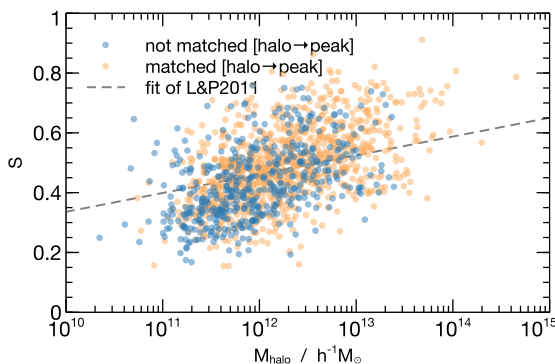


Figure 9. Joint distribution of proto-halo mass and sphericity S (equation 25) in the matched (orange) and unmatched (blue) cases. There is a strong trend of sphericity with mass, as noted in Figure 6. Apart from this, however, there is no significant difference between the sphericities of matched and unmatched proto-haloes. The dashed line, which is somewhat shallower than the measured mass trend, shows the linear fit to corresponding measurements in CDM simulations presented by Ludlow & Porciani (2011a).

were split into different types (see Section 2.2), the most important being “type-1” (virialized haloes) and “type-2” (objects in late stages of formation). The results above are for the 1522 “type-1” objects, while we have ignored the 438 “type-2” objects. If the latter also form from peaks, our choice of “type-1” could be a cause for concern since a peaks-based analysis such as ESP might simply not be able to distinguish between them. Indeed, we do not find a significant difference between the proto-halo regions of “type-2” and “type-1” objects. Moreover, we find that including the “type-2” objects in the analysis on the same footing as “type-1” leads to a larger number (1097) of matched ESPEaks, meaning that 87% of our ESPEaks can be matched to *some* object that is either about to or has completely virialized. (The fraction of *unmatched* proto-halo patches is now $\sim 44\%$, as compared with 33% when using only “type-1”. This is largely simply because the combined number of “type-1” and “type-2” objects (1960) is significantly larger than that of the ESPEaks, which can only be accommodated in the ESP calculation by lowering the collapse threshold.)

Interestingly, AHA13 found that the transition between “type-2” and “type-1” occurs fast and is associated with a rapid mass growth, bringing a “type-2” object to a mass around or above the half-mode mass by the time it has virialized and thus turned into a “type-1” object. This is consistent with the picture that power spectra with steeper (effective) slopes show enhanced accretion rates (Lacey & Cole 1993, 1994). These observations suggest that the excursion set calculation could be failing because it is unable to capture the quick mass growth that “type-1” objects experience around the half-mode mass scale, possibly due to an incorrect prediction of *collapse-time* for a given peak-patch. The rapid transition between these two types of objects means that even small errors in predicting the collapse-time could dramatically alter the predicted locations and masses of fully virialized haloes. As we discuss in the next Section, such an error can also account for the correlations we find between proto-halo curvature and mass/location mismatches⁵.

5 ANALYTICAL RESULTS

In this section we use the results of our numerical study to motivate an analytical approximation which captures the sharp cut-off in the mass function better than the standard ESP calculation.

⁵ The unmatched proto-haloes also have significantly larger densities than the matched ones. As an additional direct test of the barrier hypothesis, we have performed walks centred at the *known* proto-halo centres. This gives us another catalog of masses and corresponding Lagrangian properties, and removes some of the ambiguity associated with off-centring effects which are one potential cause of the low matched fraction we reported above. When using this algorithm, we find that almost all the proto-haloes that were unmatched as per our earlier algorithm are now assigned masses significantly *larger* than their true mass. This is consistent with their larger overdensities compared to the matched proto-haloes: larger local overdensities imply that walks centred at these locations will cross the excursion set barrier at larger mass scales. There is, however, no obvious reason for this trend, and we return to this point in Section 6.

5.1 A possible explanation for the mis-match between ESPEaks and proto-haloes

The behaviour discussed above might be explained if, at small masses, the algorithm systematically overpredicts the *time* at which a given peak-patch should collapse. This is because a patch that collapses earlier than predicted will have time to accrete mass by the time of interest, and will consequently have a larger mass than predicted. As noted by AHA13, low mass WDM haloes tend to grow much more rapidly than their high mass counterparts, so even a small error in collapse-time could have a dramatic impact on the predicted mass function. This is further corroborated by our observation in Section 4.3 that the assignment of peaks to either virialized haloes or objects in the late stages of formation is somewhat uncertain.

Let us suppose that there is in fact such a systematic uncertainty in collapse-time. This is not an unreasonable assumption; similar effects have been noticed and discussed by other authors (Monaco 1999; Giocoli et al. 2007) in the case of CDM. Such effects could arise due to simplifying choices made in models such as ellipsoidal collapse (see Appendix B for a justification), as well as due to other physical mechanisms such as assembly-bias⁶. Can this explain the orders-of-magnitude mass increases that are required to go from the ESPEaks mass function to the halo mass function? To see why this is indeed the case, consider the following.

A collapse-time uncertainty can be interpreted as introducing a *second* barrier in the problem, in the sense that if a patch has been identified at mass m using the barrier B (in this case the one in equation 28) it must then be allowed to accrete until mass M when its density δ_{patch} reaches the “mass re-assignment” barrier $B_{\text{mra}} = B - \Delta B$, where ΔB is positive if the original collapse-time prediction was an overestimate. Figure 10 illustrates the point. Since TopHat/Gaussian filtering induces strong correlations between walk heights, the scale M at which δ_{patch} reaches B_{mra} is essentially determined by the walk height and slope at scale m . The height at m is just $B(m)$, and in the excursion set peaks picture the walk slope is strongly correlated with the peak curvature, so that $d\delta/d\sigma_0 \approx x/\gamma$ (this relation is exact for Gaussian filtering). The model therefore says that sharper peaks will tend to have more closely matched masses, while shallower peaks will have larger mismatches.

Note also that the WDM transfer function leads to a “freeze-out” of all power spectrum integrals as $m \rightarrow 0$ (c.f. Section 2.3). This will amplify the above effect at small masses where a small change in σ_0 will imply a huge change in m . Additionally, peaks of lower significance will tend to be shallower on average, and this will also systematically enhance the mismatch at low masses.

If this idea is correct, then we should see two effects. Firstly, matched proto-halo patches with lower curvatures should have

⁶ It is also worth noting that Monaco (1999) discussed the difference between what he called orbit-crossing (first-axis collapse) and multi-streaming (last-axis collapse). Standard ellipsoidal collapse models employ the latter as the criterion for collapse, and Monaco argued why one might then expect to correctly predict the locations of collapse but not the halo masses. In particular, he argued that orbit crossing may be a better indicator of halo mass. The semi-analytic code PINOCCHIO (Monaco et al. 2002, 2013) uses orbit-crossing as a key ingredient in halo identification, and as a follow-up it would be very interesting to check how accurately PINOCCHIO describes the mass function cut-off in WDM cosmologies.

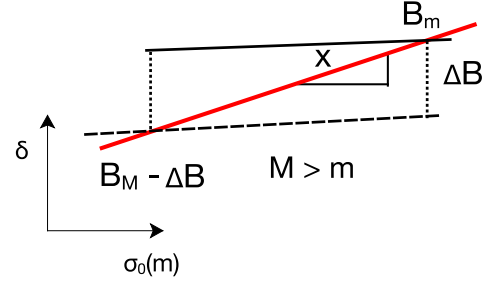


Figure 10. An illustration of mass reassignment: An ESPEak is identified at scale m with height $\delta = B_m$ and curvature x . If the collapse-time prediction in the dynamical model is a systematic overestimate, the ESPEak is allowed to accrete mass for a time Δt which translates into a lowering of the barrier by ΔB . Since the random walk describing the ESPEak has strongly correlated steps, the accretion occurs along essentially a straight line of slope $\dot{\delta} = x/\gamma$ in the δ - σ_0 plane. This sets the mass scale $M > m$ which is ultimately assigned to this ESPEak.

preferentially larger mass mismatches and vice-versa; and secondly, unmatched proto-haloes must have preferentially low values of curvature (a shallow walk that “freezes” before crossing an incorrect barrier will not register as a potential halo). Figure 7 is consistent with the first effect, while the second effect is seen quite clearly in Figure 8 (see also the discussion in Section 4.5).

In the following, we will therefore assume that the idea of a collapse-time overprediction is correct, and leave for future work a more detailed modelling of the scatter of the mass mismatch by including, e.g., the effect of proto-halo sphericity. We can implement the notion of a second barrier in the ESP calculation as follows. We start by recapitulating the calculation of Paranjape et al. (2013), which we refer to as standard ESP.

5.2 Standard excursion set peaks

The predicted number density of ESPEaks in this calculation can be formally written as

$$dn/d \ln m = \int \mathcal{D}\mathbf{X} \mathcal{N}_{\text{pk}}(\mathbf{X}) \delta_{\text{D}}(\ln m - \ln \bar{m}(\sigma_0)), \quad (30)$$

where the integral is over all relevant variables (e.g., peak density, curvature, shear, etc.) and the function $\mathcal{N}_{\text{pk}}(\mathbf{X})$ incorporates the intrinsic (Gaussian) probability of these variables, as well as the peaks constraint (26) and the excursion set constraint which requires first crossing of the chosen barrier. The latter means that the integration variables also include σ_0 , and the Dirac delta $\delta_{\text{D}}(\ln m - \ln \bar{m}(\sigma_0))$ then assigns the mass according to the first-crossing scale σ_0 , where $\bar{m}(\sigma_0)$ is the inverse function of $\sigma_0(m)$ (see Appendix A for details).

In the calculation of Paranjape et al. (2013), the barrier was assumed to be $B = \delta_c + \beta\sigma_0$ where β is a stochastic variable whose distribution was motivated by the CDM measurements of Robertson et al. (2009) and was assumed independent of the tensors $\partial_{ij}\psi$ and $\partial_{ij}\delta$. In particular, $p(\beta)$ was taken to be Lognormal with mean 0.5 and variance 0.25. The resulting mass function is then (equations 12 and 13 of Paranjape et al. 2013)

$$dn_{\text{ESPstd}}/d \ln m = \nu \mathcal{N}_{\text{ESPstd}}(\nu) |d \ln \sigma_0/d \ln m|, \quad (31)$$

with $\nu \equiv \delta_c(z)/\sigma_0(m)$ and

$$\nu \mathcal{N}_{\text{ESPstd}}(\nu) = \int d\beta p(\beta) \frac{e^{-(\nu+\beta)^2/2}}{\sqrt{2\pi} V_*} \int_{\beta\gamma}^{\infty} dx (x/\gamma - \beta) F(x) \times p_G(x - \beta\gamma - \gamma\nu; 1 - \gamma^2), \quad (32)$$

where $F(x)$ is the BBKS curvature function (equation A11) and $p_G(y - \mu; \Sigma^2)$ is a Gaussian in the variable y with mean μ and variance Σ^2 . The solid black curve in Figure 1 shows this expression⁷, using the WDM transfer function (1).

In order to implement the barrier (28), we must account for the correlation between the eigenvalues of the velocity shear $\partial_{ij}\psi$ and those of the density Hessian $\partial_{ij}\delta$. Although this is straightforward in principle, in practice the misalignment between these tensors turns out to be cumbersome to deal with (see Appendix A). We therefore explore a simpler, albeit approximate, solution. Following Sheth et al. (2001), we look for the value at which the distribution $p(Y|\delta)$ has its maximum, ignoring the peaks constraint. (This distribution can be obtained by integrating equation A3 of Sheth et al. 2001, over the prolateness, and is different from $p(Y, Z = 0|\delta)$ which is what those authors worked with.) This happens at $Y_{\text{max}} = 0.502\sigma_0 \approx 0.5\sigma_0$. We therefore look for the first crossing of the *deterministic* barrier

$$B = \delta_c + \bar{\beta}\sigma_0 = \delta_c + 0.5\sigma_0. \quad (33)$$

The dashed black curve in Figure 1 shows this expression, which amounts to replacing the integral over $\int d\beta p(\beta)$ in equation (32) with the single value $\beta = \bar{\beta} = 0.5$:

$$dn_{\text{ESPdet}}/d \ln m = \nu \mathcal{N}_{\text{ESPdet}}(\nu) |d \ln \sigma_0/d \ln m|, \quad (34)$$

with

$$\begin{aligned} \nu \mathcal{N}_{\text{ESPdet}}(\nu) &= \int_{\bar{\beta}\gamma}^{\infty} dx \mathcal{N}_{\text{ESPdet}}(\nu, x) \\ &= \frac{e^{-\frac{1}{2}(\nu+\bar{\beta})^2}}{\sqrt{2\pi} V_*} \int_{\bar{\beta}\gamma}^{\infty} dx (x/\gamma - \bar{\beta}) F(x) \\ &\quad \times p_G(x - \bar{\beta}\gamma - \gamma\nu; 1 - \gamma^2), \end{aligned} \quad (35)$$

We see that this describes the dashed blue histogram quite well (this was the result of our empirical walks algorithm for the barrier (33), see Section 4.2). Consequently, it is also not very different from the solid orange histogram, which was the result of the empirical walks using the stochastic barrier (28), as well as the standard ESP calculation (solid black curve).

A similar calculation gives the predicted distribution $p(x|\text{ESP})$ of ESPeak curvature. For the deterministic barrier

⁷ Since Paranjape et al. (2013) were interested in a CDM mass function, they used a TopHat filter to compute σ_0 but a Gaussian filter for σ_1 and σ_2 . (Recall σ_2 diverges for a TopHat filtered CDM spectrum.) The smoothing scale R_G for the latter was set by demanding $\langle \delta_G | \delta_{\text{TH}} \rangle = \delta_{\text{TH}}$, i.e. $\langle \delta_G \delta_{\text{TH}} \rangle = \sigma_0 (R_{\text{TH}})^2$. Consequently, V_* was computed using the Gaussian filter and γ was defined using mixed filtering. We used this prescription for the solid black curve in Figure 1. To keep things simple in the present work, however, we will define *all* quantities in the analytical calculation using Gaussian filtering, with the filtering scale matched to the mass using the relation mentioned above. We have checked that switching to TopHat filtering for defining σ_0 has little impact on our results. Additionally, using Gaussian filtering throughout guarantees self-consistency; e.g., the relation $d\delta/d\sigma_0 = x/\gamma$, which we use below, is exact in this case.

(33) this is

$$p(x|\text{ESPdet}) = \frac{\int d \ln \sigma_0 \nu \mathcal{N}_{\text{ESPdet}}(\nu, x)}{\int d \ln \sigma_0 \int_{\bar{\beta}\gamma}^{\infty} dx \nu \mathcal{N}_{\text{ESPdet}}(\nu, x)}, \quad (36)$$

where $\mathcal{N}_{\text{ESPdet}}(\nu, x)$ was defined in equation (35). The dashed black curve in Figure 4 shows the result; this is very similar in shape to the measured proto-halo curvature distribution but has a higher mean value.

5.3 Re-assigning mass

To implement the mass re-assignment, we modify equation (30) by writing

$$dn/d \ln M = \int \mathcal{D}\mathbf{X} \mathcal{N}_{\text{pk}}(\mathbf{X}) p(\ln M|\mathbf{X}), \quad (37)$$

where the probability distribution $p(\ln M|\mathbf{X})$ accounts for the mass re-assignment. If the re-assignment were deterministic, this distribution would be a Dirac delta centred on the appropriate re-assigned mass value. Indeed, this is precisely what equation (30) does, except that it gets the mass wrong. In practice, in addition to changing the mass, we allow for some scatter, which is more realistic and also improves the numerical stability of our calculation.

Suppose the standard calculation identifies an ESPeak and assigns it a mass m . If the collapse-time uncertainty discussed earlier leads to a barrier shift $-\Delta B$, then the strongly correlated nature of the filtered density contrasts δ at different smoothing scales means that the mass scale M at the new barrier satisfies

$$B_M - \Delta B = B_m + \frac{x_m}{\gamma_m} (\sigma_{0M} - \sigma_{0m}), \quad (38)$$

where the subscript indicates smoothing scale, and we approximated the walk in density $\delta(\sigma_0)$ as a straight line with slope $d\delta/d\sigma_0 = x/\gamma$. If we assume that ΔB is Gaussian distributed with mean $\overline{\Delta B}$ and variance $\sigma_{\Delta B}^2$, and that B is given by equation (33), then we have

$$\begin{aligned} p(\sigma_{0M}|\mathbf{X}) &= \int d\Delta B p_G(\Delta B - \overline{\Delta B}; \sigma_{\Delta B}^2) \theta_H \left(\sigma_{0m} - \frac{\Delta B}{x_m/\gamma_m - \bar{\beta}} \right) \\ &\quad \times \delta_D \left(\sigma_{0M} - \sigma_{0m} + \frac{\Delta B}{x_m/\gamma_m - \bar{\beta}} \right) \\ &= \theta_H(\sigma_{0M}) (x_m/\gamma_m - \bar{\beta}) \\ &\quad \times p_G \left((x_m/\gamma_m - \bar{\beta})(\sigma_{0m} - \sigma_{0M}) - \overline{\Delta B}; \sigma_{\Delta B}^2 \right) \end{aligned} \quad (39)$$

where the Heaviside function $\theta_H(\dots)$ ensures that $\sigma_{0M} > 0$. The cumulative probability $p(> \ln M|\mathbf{X})$ satisfies

$$\begin{aligned} p(> \ln M|\mathbf{X}) &= p(< \sigma_{0M}|\mathbf{X}) \\ &= \frac{1}{2} \left[\text{erfc} \left(\frac{(x_m/\gamma_m - \bar{\beta})(\sigma_{0m} - \sigma_{0M}) - \overline{\Delta B}}{\sqrt{2} \sigma_{\Delta B}} \right) \right. \\ &\quad \left. - \text{erfc} \left(\frac{(x_m/\gamma_m - \bar{\beta})\sigma_{0m} - \overline{\Delta B}}{\sqrt{2} \sigma_{\Delta B}} \right) \right] \end{aligned} \quad (40)$$

The mass function with re-assigned masses then becomes

$$\begin{aligned} \frac{dn}{d \ln M} &= \int d \ln \sigma_{0m} \frac{e^{-B_m^2/(2\sigma_{0m}^2)}}{\sqrt{2\pi} V_{*m}} \int_{\bar{\beta}\gamma_m}^{\infty} dx (x/\gamma_m - \bar{\beta}) \\ &\quad \times F(x) p_G \left(x - \frac{\gamma_m B_m}{\sigma_{0m}}; 1 - \gamma^2 \right) p(\ln M|\mathbf{X}). \end{aligned} \quad (41)$$

Were we to account for the full stochasticity of B using equation (28), the expression for the mass function in equation (41) would have an additional integral over Y , and the integrand, including the distribution $p(\ln M|\mathbf{X})$, would be more complicated. However, since the mass function without mass re-assignment and with $\beta = \bar{\beta} = 0.5$ describes the results of the empirical walks with barrier (28) quite well (c.f. discussion below equation 33), we will continue to ignore this inherent stochasticity due to the ellipticity Y .

5.4 An explicit example

The distribution of ΔB will in general depend on the scale m at which the ESPeak is originally identified; we know that at large m the mass assignment is essentially correct, with small scatter, while there is a trend towards underpredicting masses at small m . Since there is little guidance from theory for the actual values of $\overline{\Delta B}$ and $\sigma_{\Delta B}$, we have left these as free parameters, except for requiring that they become numerically small for large m or small σ_{0m} . The following is intended as a proof of principle, and we leave a more detailed analysis and estimate of $\overline{\Delta B}$ to future work.

We compare σ_{0m} with the scale $\sigma_{0,\text{turn}}$ which we define as the scale at which the Jacobian between σ_0 and m becomes small. In particular, we set

$$|\mathrm{d} \ln \sigma_0 / \mathrm{d} \ln m|_{\text{turn}} = 0.1. \quad (42)$$

In practice, for $m_{\text{dm}} = 0.25 \text{keV}$ this occurs at $m \simeq 3.2 \times 10^{12} h^{-1} M_{\odot}$ which is close to the half-mode mass scale $M_{\text{hm}} \simeq 3 \times 10^{12} h^{-1} M_{\odot}$. We have chosen this definition since it remains well-behaved in the CDM limit as well, whereas the half-mode mass goes to zero in that case. The choice of 0.1 as the threshold in equation (42) is, however, arbitrary.

The solid blue curve in Figure 11 shows the result of using equation (41) after setting

$$\overline{\Delta B} = 5\sigma_{\Delta B} = 0.175 \times (\sigma_{0m}/\sigma_{0,\text{turn}})^3. \quad (43)$$

The shape of the turnover is quite sensitive to the value of $\overline{\Delta B}$, less so to $\sigma_{\Delta B}$. The numerical values of the amplitude and exponent in the expression on the right are quite degenerate. With these settings, the ESP mass function with re-assigned masses gives a fairly good description of the halo masses in the simulation (histogram). For comparison, the Figure also shows the ESP mass function using the barrier (33) but *before* mass re-assignment (dashed black; this is the same as in Figure 1), and the Tinker et al. (2008) fitting function (dotted black). Additionally, the dot-dashed blue curve shows the sharp- k excursion set fit proposed by Schneider et al. (2013) to their simulations. (For the latter we used their spherical collapse fit, setting their $q = 1$ and $c = 2.7$, which gives an excellent description of their $z = 0$ haloes at $m < 10^{15} h^{-1} M_{\odot}$.)

The top panel of Figure 12 shows our analytical mass function at $z = 0$ with masses re-assigned using the same parameter values as in equation (43) for three different values of dark matter particle mass m_{dm} (solid curves). We also show the corresponding curves fit by Schneider et al. (2013), again using their spherical collapse fit (dot-dashed curves). In the bottom panel we show our analytical prediction for $m_{\text{dm}} = 0.25 \text{keV}$, now for three different redshifts. The solid curves marked 0.25keV in both panels are identical, and the same as the solid blue curve in Figure 11.

We have chosen to model the mass re-assignment on an object-by-object basis, since this is what our empirical walks

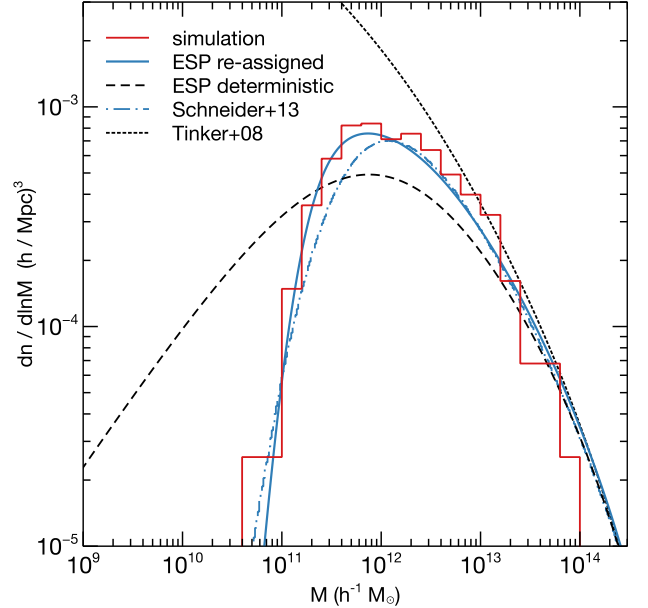


Figure 11. Halo mass functions: the solid red histogram and dashed black curve are the same as in Figure 1 and show, respectively, the mass function of haloes in the simulation and the ESP prediction (34) using the deterministic barrier (33). The solid blue curve shows the result of re-assigning masses using equation (41), with parameter values from equation (43). For comparison, the dot-dashed blue curve shows the fit based on sharp- k filtering presented by Schneider et al. (2013), their spherical collapse fit with $q = 1$ and $c = 2.7$, which is a good description of the mass function measured in their simulation. The dotted black curve shows the Tinker et al. (2008) fitting form.

seem to require. This means that equation (37) preserves the total number density of haloes, which is returned as $2.69 \times 10^{-3} (h/\text{Mpc})^3$. (As noted earlier, this is somewhat lower than the measured number density of haloes, $2.97 \times 10^{-3} (h/\text{Mpc})^3$.) In contrast, the *mass fraction* in collapsed objects given by

$$f_{\text{coll}} = \int \mathrm{d} \ln M (M/\bar{\rho}) \mathrm{d}n/\mathrm{d} \ln M, \quad (44)$$

is not held fixed during the re-assignment, which is obvious since the calculation allows haloes to accrete more mass than is predicted in the standard ESP treatment. The values for f_{coll} returned by the analytical calculation before and after mass re-assignment are, respectively, 0.19 and 0.23. In comparison, the mass fraction in actual haloes is 0.18, but note that this number can fluctuate due to sample variance effects at the high-mass end.

5.5 Consequences for CDM

The predictions of the ellipsoidal collapse model, augmented by a systematic uncertainty in mass assignment, accurately describe the WDM mass function. By the logic discussed earlier, the same expressions with the CDM transfer function should describe the CDM mass function. In particular, the half-mode mass scale for CDM is small enough that, in practice, every halo has a virialized progenitor. This means that the effects of collapse-time uncertainty – which were very pronounced around the half-mode mass of WDM due to the rapid growth of those objects – are now essentially an uncertainty in the time of major mergers, and consequently the associated mass

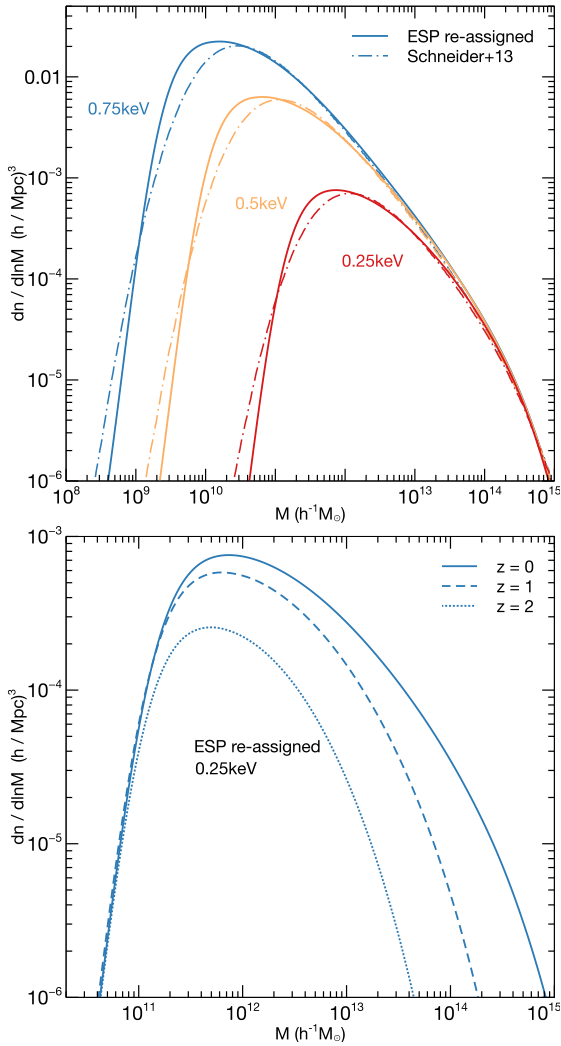


Figure 12. (*Top panel:*) Analytical halo mass functions for different values of m_{dm} ; 0.25keV (red), 0.5keV (yellow) and 0.75keV (blue). The solid curves show the result of re-assigning masses in the ESP calculation using equation (41), with parameter values from equation (43). For comparison, the dot-dashed curves show the fit based on sharp- k filtering presented by Schneider et al. (2013), their spherical collapse fit with $q = 1$ and $c = 2.7$, which is a good description of the mass function measured in their simulation. (*Bottom panel:*) ESP mass functions with re-assigned masses at three different redshifts.

mismatch must be significantly smaller. We see in Figure 13 that this is indeed the case for masses $m \gtrsim 10^{11} h^{-1} M_{\odot}$. It is also reassuring to note that changing the value of $\overline{\Delta B}$ in the CDM case has much less effect on the mass function at $m \gtrsim 10^{11} h^{-1} M_{\odot}$ than in the WDM case. E.g., we have checked that increasing the amplitude in equation (43) by a factor 1.5 or changing the exponent from 3 to 2 both lead to $\lesssim 3\%$ changes in the CDM mass function for $m \gtrsim 10^{11} h^{-1} M_{\odot}$.

At lower masses our specific implementation of mass re-assignment predicts a factor ~ 2 larger number of haloes than expected from the mass function fit by Tinker et al. (2008). This behaviour of the re-assigned mass function at low masses is not very robust, however; it is sensitive to the specific numerical choice in equation (42). It is possible to adjust this number (and those in equation 43) to simultaneously get a good match to the CDM and WDM simulations, although we have not

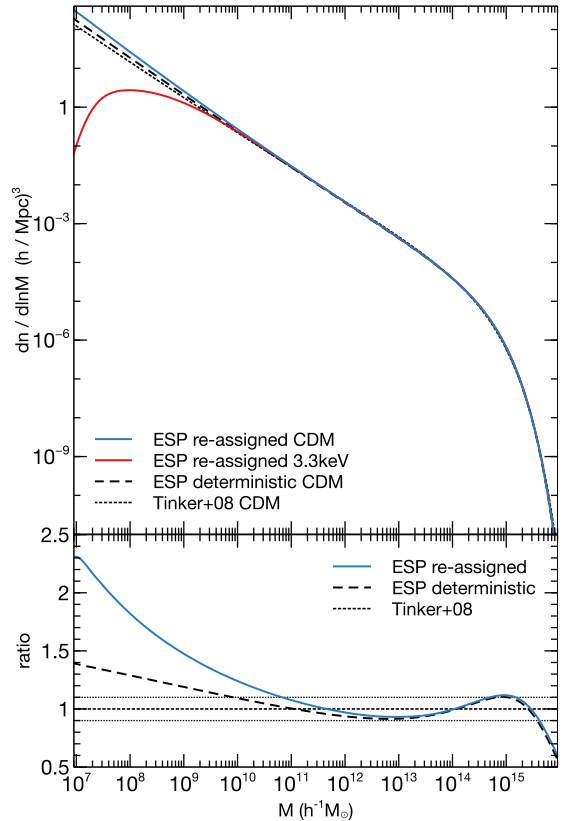


Figure 13. ESP mass function predictions for CDM using the deterministic barrier (33) (dashed black) and after re-assigning masses (solid blue). The dotted black curve shows the Tinker et al. (2008) fitting form, which was calibrated over a range between $\sim 10^{10.5} h^{-1} M_{\odot}$ and $\sim 10^{15.5} h^{-1} M_{\odot}$. The solid red curve shows the prediction, after mass re-assignment, for a “realistic” WDM particle candidate with $m_{\text{dm}} = 3.3\text{keV}$. In all cases the mass re-assignment parameters are the same as in equation (43). The lower panel shows the ratio of the CDM predictions to the Tinker et al. fit.

pursued this exercise here. One must also keep in mind that the Tinker et al. (2008) fit was calibrated for masses between $\sim 10^{10.5} h^{-1} M_{\odot}$ and $\sim 10^{15.5} h^{-1} M_{\odot}$.

In other words, our proposed modifications to the ESP calculation not only correctly describe the sharp turn in the WDM mass function, but also describe the CDM mass function with the same accuracy as the standard ESP calculation of Paranjape et al. (2013). For CDM we have also checked that the linear Lagrangian halo bias predicted by this model (not shown) matches measurements in CDM simulations (Tinker et al. 2010) with the same accuracy as the Paranjape et al. (2013) calculation. However, as noted earlier, low mass in WDM does not mean low significance, and, in principle, low significance CDM haloes could be different from low mass WDM haloes. Testing this would need high resolution CDM simulations, or WDM simulations with a slightly larger mass such as $m_{\text{dm}} \sim 0.5\text{keV}$.

6 DISCUSSION AND CONCLUSIONS

Can we predict where and when haloes form? In this paper, we have thoroughly evaluated our ability to predict the abundance

of collapsed objects by performing an in-depth analysis of the properties of the initial density field at the locations where collapse occurs in numerical simulations. To accomplish this, we used a perturbation spectrum with a small-scale cut-off such as those arising in WDM cosmologies. As discussed in Section 2, the resulting suppression of low mass haloes provides powerful additional leverage which is absent in the CDM case.

Numerical simulations have traditionally had great difficulty in making a prediction for the abundance of haloes in such a scenario due to the artificial fragmentation of filaments – a problem that has only recently been overcome by Angulo et al. (2013, AHA13). As a consequence, we were in the unique situation of being able to perform a thorough comparison between this numerical experiment and the mass function predicted from excursion set theory, by analysing the properties of haloes on an object-by-object basis. We summarize our results below, and discuss some outstanding issues.

It is well known that the standard excursion set approach predicts a mass function that is completely inconsistent with the numerical results (see, e.g., Schneider et al. 2012, and also our Figure 1). We showed that the inclusion of the peaks constraint in excursion sets (Musso & Sheth 2012; Paranjape & Sheth 2012; Paranjape et al. 2013) leads to a turn-over in the mass function as well as an overall number of collapsed objects that is consistent with the simulation results. However, it also predicts masses around and below the half-mode mass scale that are significantly smaller than those measured in the simulation, leading to a small-mass slope of the mass function ($dn/d \ln m \sim m^{2/3}$) that is inconsistent with that found from the simulation (c.f. Figure 1). This prediction is remarkably robust against changing details of the calculation such as the shape and stochasticity of the barrier.

We next investigated the origin of this discrepancy between simulation and theoretical predictions. In particular, we analysed the Lagrangian properties of “proto-haloes” (the initial locations of groups of particles which are eventually identified as haloes in the simulation), and also performed empirical excursion set peak walks in the initial density field used in the simulation. We can summarize our findings as follows:

1. All haloes in the simulation are consistent with forming near peaks in the initial density field (Figure 4).
2. The overdensities of proto-haloes are strongly correlated with their shear ellipticities, but show no correlation with the shear prolateness (Figure 5). The former is expected from arguments based on ellipsoidal collapse dynamics, while the latter is not (compare equation 28 with equation 29). The fact that the proto-halo overdensity has no correlation with its prolateness is intimately connected with the distribution of individual shear eigen-values and hence with the dynamical ordering of the collapse times of each (Ludlow & Porciani 2011a; Despali et al. 2013). It will be interesting to find a dynamical model that is consistent with our results, perhaps along the lines presented by Ludlow & Porciani (2011a).
3. The number of “ESPeaks” (1261) identified by our empirical algorithm (Section 4.1) is reasonably close to the actual number of proto-haloes (1522).
4. A significant fraction (74%) of ESpEaks can be matched to actual proto-haloes, while 64% of the proto-haloes can be matched to ESpEaks (details in Section 4.3).
5. The curvatures of these matched objects are significantly higher, and their overdensities significantly lower, than those

of proto-haloes and ESpEaks that could *not* be matched to each other (Figure 8).

6. Most strikingly, the masses of ESpEaks are systematically lower than the proto-halo masses. This is true for both matched and unmatched objects (respectively, top and bottom panels of Figure 7). Since the ESpEak mass function is very well described by the ESP calculation (Figure 1), this fully accounts for the discrepancy between the ESP halo mass function and that measured in the simulation.
7. For matched objects, the mismatch in mass assignment correlates with proto-halo curvature (Figure 7), while the scatter in the mass mismatch correlates with proto-halo shape (Figure 6).
8. We have checked that, apart from having larger overdensities and lower curvatures than their matched counterparts, the *unmatched* proto-haloes do not appear to be special in any other property related to the velocity shear, density Hessian or moment of inertia.
9. If we also include in the analysis objects in late stages of formation (“type-2” in AHA13), 87% of the ESpEaks can be matched to proto-haloes (although the fraction of unmatched proto-haloes is now larger, largely because the total number of proto-haloes increases). These “type-2” objects are known to be undergoing rapid mass growth (AHA13).

Based on these results, we argued that the likely cause for the observed mass mismatch between ESpEaks and proto-haloes is a systematic overprediction of the collapse-time for a given perturbation. We then showed how such an uncertainty can be accounted for and corrected in the excursion set language (Section 5.1 and Figure 10), and presented an explicit example of such a correction which describes the numerical WDM results very well (Figures 11 and 12). As an important consistency check, we also showed that the same model gives an accurate description of the CDM mass function, with the simple replacement of the WDM initial power spectrum with that of CDM (Figure 13).

We emphasize that our solution works because it explicitly alters the mass assignment step of the ESP calculation, in our case by introducing a second barrier. Simply introducing new statistical variables defined by smoothing the initial density field in a single-barrier calculation (say, by setting $B \rightarrow \delta_c + Y + x\sigma_0$) would not work, because the predicted mass function in this case would still behave as $dn/d \ln m \sim m^{2/3}$ at low masses, as discussed in Section 2.3. At the heart of this issue is the difference between the physics of individual halo formation and the statistics of the initial density field: mismatches in collapse time predictions are primarily a physical, not statistical, problem. In CDM, since the $\sigma_0(m)$ relation is always steep, errors in the physical collapse model can be accommodated by altering the statistical modelling (e.g., by changing the barrier shape as a function of σ_0 , or by introducing stochasticity in the barrier). WDM, on the other hand, presents us with a situation where such solutions no longer work since the $\sigma_0(m)$ relation “freezes out” at small masses (Figure 2). A full solution of the problem would likely involve a single barrier with an explicit dependence on mass (rather than σ_0) which is fixed by an accurate model of collapse.

Our work can be extended in several directions which could yield clues towards building a more predictive model. Although we argued that uncertainties in collapse-time can easily arise in toy models such as ellipsoidal collapse, or due to assembly-bias-like effects, we have not provided conclusive evidence pinpointing a specific physical mechanism. Furthermore, the

proto-halo curvatures we measure are significantly lower than the simplest ESP prediction (Figure 4). While this might be partially accounted for by the mass re-assignment, it is not clear whether there is a deeper reason for this discrepancy. Also, the scatter in ESpeak mass at fixed halo mass for matched objects correlates strongly with the proto-halo shapes (Figure 6). Our mass re-assignment currently incorporates only curvature, and it will be interesting to additionally account for proto-halo shapes. The overdensities of unmatched proto-haloes have a significantly higher tail than that of matched objects (Figure 8). This could be indicating that low mass WDM haloes can form near density peaks without necessarily satisfying the excursion set peaks constraints; e.g., there could be some other criterion for a sufficiently overdense patch to virialize. One way forward would be to analyse the local environments of these unmatched objects to look for peculiarities. Finally, while our chosen particle mass of $m_{\text{dm}} = 0.25\text{keV}$ is untenably warm, any realistic massive dark matter candidate would lead to very similar phenomenology around its half-mode mass scale, and our analysis would be relevant whenever this scale can be numerically resolved. As mentioned earlier, however, for a particle much colder than our present choice, low mass haloes will also have low *significance* ($\nu \ll 1$) which was not possible in our case, and this could lead to additional effects. Clearly, it will be of great interest to investigate these aspects further in future work.

ACKNOWLEDGEMENTS

We thank Raul Angulo for providing us with the halo catalogues published in AHA13. We wish to thank him, Ravi Sheth, Tom Abel and Cristiano Porciani for insightful discussions and comments on the draft. O.H. acknowledges support from the Swiss National Science Foundation (SNSF) through the Ambizione fellowship.

REFERENCES

- Achitouv I., Rasera Y., Sheth R. K., Corasaniti P. S., 2012, ArXiv e-prints: 1212.1166
- Angrick C., Bartelmann M., 2010, *A&A*, 518, A38
- Angulo R. E., Hahn O., Abel T., 2013, *MNRAS*, 434, 3337 (AHA13)
- Appel L., Jones B. J. T., 1990, *MNRAS*, 245, 522
- Arnold V. I., Shandarin S. F., Zeldovich I. B., 1982, *Geophysical and Astrophysical Fluid Dynamics*, 20, 111
- Avila-Reese V., Colín P., Valenzuela O., D’Onghia E., Firmani C., 2001, *ApJ*, 559, 516
- Bardeen J. M., Bond J. R., Kaiser N., Szalay A. S., 1986, *ApJ*, 304, 15 (BBKS)
- Benson A. J. et al., 2013, *MNRAS*, 428, 1774
- Bode P., Ostriker J. P., Turok N., 2001, *ApJ*, 556, 93
- Bond J. R., 1989, in *Frontiers in Physics - From colliders to cosmology*, proceedings of the Lake Louise Winter Institute, Astbury A., Campbell B., Israel W., Kamal A., Khanna F., eds., pp. 182–235
- Bond J. R., Cole S., Efstathiou G., Kaiser N., 1991, *ApJ*, 379, 440
- Bond J. R., Myers S. T., 1996, *ApJS*, 103, 1 (BM96)
- Crocce M., Pueblas S., Scoccimarro R., 2006, *MNRAS*, 373, 369
- Desjacques V., 2008, *MNRAS*, 388, 638
- Despali G., Tormen G., Sheth R. K., 2013, *MNRAS*, 431, 1143
- Eisenstein D. J., Hu W., 1999, *ApJ*, 511, 5
- Eisenstein D. J., Loeb A., 1995, *ApJ*, 439, 520
- Eke V. R., Cole S., Frenk C. S., 1996, *MNRAS*, 282, 263
- Elia A., Ludlow A. D., Porciani C., 2012, *MNRAS*, 421, 3472
- Epstein R. I., 1983, *MNRAS*, 205, 207
- Fakhouri O., Ma C.-P., 2010, *MNRAS*, 401, 2245
- Gao L., Springel V., White S. D. M., 2005, *MNRAS*, 363, L66
- Giocoli C., Moreno J., Sheth R. K., Tormen G., 2007, *MNRAS*, 376, 977
- Gunn J. E., Gott, III J. R., 1972, *ApJ*, 176, 1
- Hahn O., Abel T., 2011, *MNRAS*, 415, 2101
- Hahn O., Abel T., Kaehler R., 2013, *MNRAS*
- Hahn O., Porciani C., Dekel A., Carollo C. M., 2009, *MNRAS*, 398, 1742
- Hanami H., 2001, *MNRAS*, 327, 721
- Henry J. P., 2000, *ApJ*, 534, 565
- Kitaura F.-S., Heß S., 2013, *MNRAS*, 435, L78
- Komatsu E. et al., 2011, *ApJS*, 192, 18
- Lacey C., Cole S., 1993, *MNRAS*, 262, 627
- Lacey C., Cole S., 1994, *MNRAS*, 271, 676
- Laureijs R. et al., 2011, ArXiv e-prints: 1110.3193
- Lavaux G., Wandelt B. D., 2010, *MNRAS*, 403, 1392
- Lovell M. R. et al., 2012, *MNRAS*, 420, 2318
- Lovell M. R., Frenk C. S., Eke V. R., Jenkins A., Gao L., Theuns T., 2013, ArXiv e-prints:1308.1399
- Ludlow A. D., Porciani C., 2011a, ArXiv e-prints: 1107.5808
- Ludlow A. D., Porciani C., 2011b, *MNRAS*, 413, 1961
- Maggiore M., Riotto A., 2010, *ApJ*, 711, 907
- Manera M. et al., 2013, *MNRAS*, 428, 1036
- Manrique A., Raig A., Solanes J. M., Gonzalez-Casado G., Stein P., Salvador-Sole E., 1998, *ApJ*, 499, 548
- Marín F. A. et al., 2013, *MNRAS*, 432, 2654
- Melott A. L., 2007, ArXiv e-prints: 0709.0745
- Monaco P., 1999, in *Astronomical Society of the Pacific Conference Series*, Vol. 176, *Observational Cosmology: The Development of Galaxy Systems*, Giuricin G., Mezzetti M., Salucci P., eds., p. 186
- Monaco P., Sefusatti E., Borgani S., Crocche M., Fosalba P., Sheth R. K., Theuns T., 2013, *MNRAS*, accepted
- Monaco P., Theuns T., Taffoni G., 2002, *MNRAS*, 331, 587
- Musso M., Sheth R. K., 2012, *MNRAS*, 423, L102
- Musso M., Sheth R. K., 2013, ArXiv e-prints: 1306.0551
- Padmanabhan T., 1993, *Structure Formation in the Universe*, ISBN 0521424860. Cambridge University Press, Cambridge, UK
- Paranjape A., Lam T. Y., Sheth R. K., 2012, *MNRAS*, 420, 1429
- Paranjape A., Sheth R. K., 2012, *MNRAS*, 426, 2789
- Paranjape A., Sheth R. K., Desjacques V., 2013, *MNRAS*, 431, 1503
- Peacock J. A., Heavens A. F., 1990, *MNRAS*, 243, 133
- Porciani C., Dekel A., Hoffman Y., 2002, *MNRAS*, 332, 339
- Press W. H., Schechter P., 1974, *ApJ*, 187, 425
- Robertson B. E., Kravtsov A. V., Tinker J., Zentner A. R., 2009, *ApJ*, 696, 636
- Scannapieco E., Barkana R., 2002, *ApJ*, 571, 585
- Schneider A., Smith R. E., Macciò A. V., Moore B., 2012, *MNRAS*, 424, 684
- Schneider A., Smith R. E., Reed D., 2013, *MNRAS*, 433, 1573
- Scoccimarro R., Sheth R. K., 2002, *MNRAS*, 329, 629
- Sheth R. K., 1998, *MNRAS*, 300, 1057

- Sheth R. K., Mo H. J., Tormen G., 2001, MNRAS, 323, 1 (SMT01)
- Sheth R. K., Tormen G., 2004, MNRAS, 350, 1385
- Tassev S., Zaldarriaga M., Eisenstein D. J., 2013, JCAP, 6, 36
- Tinker J., Kravtsov A. V., Klypin A., Abazajian K., Warren M., Yepes G., Gottlöber S., Holz D. E., 2008, ApJ, 688, 709
- Tinker J. L., Robertson B. E., Kravtsov A. V., Klypin A., Warren M. S., Yepes G., Gottlöber S., 2010, ApJ, 724, 878
- van de Weygaert R., Bertschinger E., 1996, MNRAS, 281, 84
- Viel M., Becker G. D., Bolton J. S., Haehnelt M. G., 2013, Phys. Rev. D, 88, 043502
- Wang J., White S. D. M., 2007, MNRAS, 380, 93
- White S. D. M., 1996, in Cosmology and Large Scale Structure, Schaeffer R., Silk J., Spiro M., Zinn-Justin J., eds., p. 349
- White S. D. M., Silk J., 1979, ApJ, 231, 1

APPENDIX A: FULLY STOCHASTIC EXCURSION SET PEAKS

Here we present some of the formal details of the excursion set peaks calculation. This will highlight the difficulty in working with the full stochasticity that must be dealt with when using a barrier such as (28), and motivate the simpler, deterministic approximation (33) used in the main text.

A1 Formal expression for mass function

In what follows, an overdot denotes a derivative with respect to σ_0 . All variables are assumed to be Gaussian filtered on a scale R which is related to the mass m through $m = (4\pi/3)\bar{\rho}R_{\text{TH}}^3$ where R_{TH} satisfies $\langle \delta_{\text{G}}(R)\delta_{\text{TH}}(R_{\text{TH}}) \rangle = \langle \delta_{\text{TH}}(R_{\text{TH}})^2 \rangle$ with the subscripts ‘G’ and ‘TH’ on δ denoting Gaussian and TopHat filtering, respectively (Paranjape et al. 2013, see also footnote 7). In practice this gives $R \approx 0.46R_{\text{TH}}$ with a slow variation. We will drop the filter subscripts below.

The ESP mass function assuming a barrier B (which can be stochastic) can be written as equation (30) where, in full glory, we have

$$\int \mathcal{D}\mathbf{X} \equiv \int d \ln \sigma_0 d^6 \psi d^6 \zeta d^3 \eta \quad (\text{A1})$$

and

$$\mathcal{N}_{\text{pk}}(\mathbf{X}) \equiv p(\partial_{ij}\psi, \partial_{ij}\delta, \nabla\delta) \mathbf{Pk}(\partial_{ij}\delta, \nabla\delta) \mathbf{ES}(\sigma_0, \{\delta, B\}). \quad (\text{A2})$$

The expression (A1) involves a total of 16 integration variables: the smoothing scale represented by σ_0 , the 6 independent components of the shear tensor $\partial_{ij}\psi$ represented by $d^6\psi$, similarly the components of the Hessian of the density $\partial_{ij}\delta$ represented by $d^6\zeta$, and finally the 3 components of the density gradient $\nabla\delta$ represented by $d^3\eta$. Strictly speaking, we must also include the scale derivative of density $\dot{\delta}$ (which will appear in the excursion set constraint) as a separate variable, but Gaussian filtering ensures that $\dot{\delta} = x/\gamma$ where x was defined in equation (15) and γ in equation (8), so this is included in $\partial_{ij}\delta$.

The raw number density of peaks $\mathcal{N}_{\text{pk}}(\mathbf{X})$ defined in equation (A2) consists of the following quantities: the joint (Gaussian) distribution function $p(\partial_{ij}\psi, \partial_{ij}\delta, \nabla\delta)$ of the shear, density gradient and density Hessian smoothed on scale R ; the peaks constraint $\mathbf{Pk}(\partial_{ij}\delta, \nabla\delta)$ which enforces $\nabla\delta = 0$ and $\zeta_i < 0$ where ζ_i are the eigenvalues of $\partial_{ij}\delta$; and the excursion

set constraint $\mathbf{ES}(\sigma_0, \{\delta, B\})$ which enforces up-crossing⁸ of the barrier by the random walk at the scale $\sigma_0(R)$. The compact notation in $\mathbf{ES}(\dots)$ hides the fact that the up-crossing condition will introduce a dependence on $\dot{\delta} = x/\gamma$ and possibly other stochastic quantities through \dot{B} . The Dirac delta in equation (30) then sets the mass to be $m = \bar{m}(\sigma_0)$ where $\bar{m}(\sigma_0)$ is the inverse function of $\sigma_0(R(m))$ as discussed above, which is straightforward to compute numerically.

In detail, following Bardeen et al. (1986, hereafter, BBKS), we have

$$\mathbf{Pk}(\partial_{ij}\delta, \nabla\delta) = \delta_{\text{D}}(\nabla\delta) |\zeta_1 \zeta_2 \zeta_3| \theta_{\text{H}}(-\zeta_3) \quad (\text{A3})$$

where we have assumed the ordering $\zeta_1 \leq \zeta_2 \leq \zeta_3$, while the excursion set constraint can be written as

$$\mathbf{ES}(\sigma_0, \{\delta, B\}) = (x/\gamma - \dot{B}) \theta_{\text{H}}(x/\gamma - \dot{B}) \delta_{\text{D}}(\mu - B/\sigma_0), \quad (\text{A4})$$

where we defined $\mu \equiv \delta/\sigma_0$. The Dirac-delta in equation (A4) enforces barrier-crossing, while the terms involving $x/\gamma = \dot{\delta}$ ensure that this is an *up*-crossing.

The intrinsic Gaussian distribution of these variables couples the tensors $\partial_{ij}\psi$ and $\partial_{ij}\delta$ through the correlation structure (van de Weygaert & Bertschinger 1996)

$$\begin{aligned} \langle \partial_{ij}\psi \partial_{kl}\psi \rangle &= \frac{\sigma_0^2}{15} (\delta_{ij}\delta_{kl} + \delta_{ik}\delta_{jl} + \delta_{il}\delta_{kj}), \\ \langle \partial_{ij}\delta \partial_{kl}\delta \rangle &= \frac{\sigma_0^2}{15} (\delta_{ij}\delta_{kl} + \delta_{ik}\delta_{jl} + \delta_{il}\delta_{kj}), \\ \langle -\partial_{ij}\delta \partial_{kl}\psi \rangle &= \frac{\sigma_1^2}{15} (\delta_{ij}\delta_{kl} + \delta_{ik}\delta_{jl} + \delta_{il}\delta_{kj}), \end{aligned} \quad (\text{A5})$$

where the δ_{ij} are Kronecker deltas, whereas the vector $\nabla\delta$ is uncorrelated with the tensors and satisfies

$$\begin{aligned} \langle \nabla_i \delta \nabla_j \delta \rangle &= \frac{\sigma_1^2}{3} \delta_{ij} \\ \langle \nabla_i \delta \partial_{jk}\psi \rangle &= 0 = \langle \nabla_i \delta \partial_{jk}\delta \rangle. \end{aligned} \quad (\text{A6})$$

A2 Consequences of misalignment

The twelve degrees of freedom in the two tensors $\partial_{ij}\psi$ and $\partial_{ij}\delta$ are most conveniently organised as the three eigenvalues of each, the three relative Euler angles between their respective eigenvectors, and three additional Euler angles that fix the orientation of one of them with respect to the chosen basis.

The correlation structure between the tensors $\partial_{ij}\psi$ and $\partial_{ij}\delta$ implies that, in a generic realisation of the field, they will be misaligned. I.e., although they are strongly correlated (with correlation coefficient γ), their respective eigenvectors will not be parallel (see, e.g., Desjacques 2008; Lavaux & Wandelt 2010; Despali et al. 2013). The misalignment is captured by the three relative Euler angles, and these must be marginalised over (the other three angles never appear in the distribution due to statistical isotropy, and can be trivially marginalised over.). The effect of this marginalisation is to introduce a nontrivial coupling between the anisotropic combinations of eigenvalues of the two tensors. So if we define y and z as in equations (19) and (20) then, as shown in an elegant calculation by Desjacques (2008), the marginalisation over Euler angles will introduce terms involving products between at least one of $\{(y+z), (3y-z)\}$ and at least one of $\{(Y+Z)/\sigma_0, (3Y-Z)/\sigma_0\}$

⁸ Musso & Sheth (2012, 2013) discuss why up-crossing is a sufficiently accurate approximation to first-crossing for walks with correlated steps.

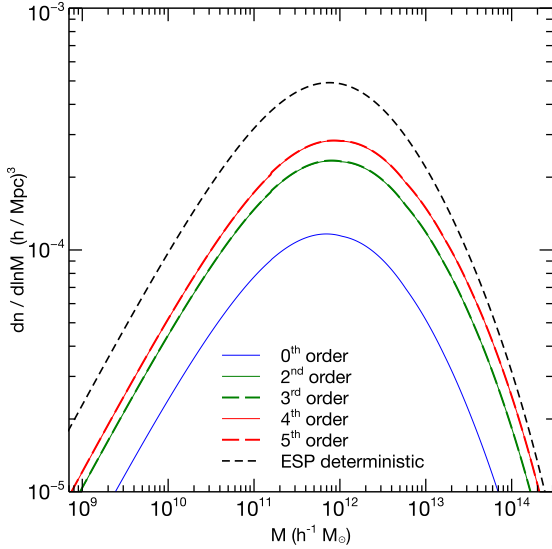


Figure A1. Accounting for the effects of stochasticity: ESP mass function predictions for WDM using the stochastic barrier (28) and the approximation $\dot{Y} = y/\gamma$ (see text for details). From bottom to top, the solid curves show the result of keeping the 0th, 2nd and 4th order terms in equation (A9), while the dashed curves (almost indistinguishable from the upper solid curves) include the 3rd and 5th order terms. The upper short-dashed black curve is the same as in Figure 1 and shows the ESP calculation using the deterministic barrier (33), which gives a very good description of the ESPEaks mass function (solid orange histogram in Figure 1) obtained with the stochastic barrier (28). While the odd order terms do not contribute significantly to the stochastic calculation, the even order terms have clearly not converged – the 4th order term gives a significant contribution compared to the 2nd order calculation.

where Y and Z were defined in equations (17) and (18), respectively. This is quite different from the coupling between the isotropic variables x and μ through the familiar Gaussian term $\sim e^{-(x-\gamma\mu)^2/2(1-\gamma^2)}$ that appears in the BBKS calculation.

This anisotropic coupling is irrelevant if we were to ignore the excursion set constraint $\mathbf{ES}(\dots)$ in equation (A2) or if the barrier B in $\mathbf{ES}(\dots)$ did not depend on any of the anisotropic variables $\{y, z, Y, Z\}$ (an example would be the barrier used by Paranjape et al. 2013), since in these cases one could marginalise over, e.g., Y and Z to recover expressions similar to those analysed by BBKS (note that ignoring the excursion set constraint altogether would give back the BBKS calculation exactly). In the case of the barrier (28), however, the calculation will involve integration of a term like $\sim p(\lambda|\zeta)e^{-(\mu+Y/\sigma_0-\gamma x)^2/2(1-\gamma^2)}$ over Y and Z , where the distribution $p(\lambda|\zeta)$ of the eigenvalues of $\partial_{ij}\psi$ given the eigenvalues of $\partial_{ij}\delta$ is given by equation (22) of Desjacques (2008).

This is not all, however. The excursion set constraint also involves the derivative \dot{B} , which in this case would lead to a term \dot{Y} . For Gaussian filtering, it is easy to check that the individual components of $\partial_{ij}\psi$ and $\partial_{ij}\delta$ are related by

$$d(\partial_{ij}\psi)/d\sigma_0 = -(\partial_{ij}\delta)/(\gamma\sigma_2), \quad (\text{A7})$$

whose trace gives the relation $\dot{\delta} = x/\gamma$ quoted earlier. If the tensors were perfectly aligned, this would also imply $\dot{Y} = y/\gamma$. In the general case, however, \dot{Y} depends on the eigenvalues of $\partial_{ij}\delta$ and the relative Euler angles between the two tensors in a highly nonlinear way. Using the ellipsoidal collapse barrier (29) would make things even more complicated.

As an example, consider using the barrier (28) with the approximation $\dot{Y} = y/\gamma$ but otherwise assuming a generic misalignment between the tensors. In this case, after a BBKS-like calculation, the mass function (with or without non-standard mass assignment) becomes

$$\begin{aligned} \frac{dn}{d\ln m} &= \int d\ln \sigma_0 \frac{1}{V_*} \frac{N}{\gamma} (1-\gamma)^4 \\ &\times \int d\tilde{x}d\tilde{y}d\tilde{z} \chi(\tilde{x}, \tilde{y}, \tilde{z}) \int d\tilde{Y}d\tilde{Z} \chi(\tilde{\nu} + \tilde{Y}, \tilde{Y}, \tilde{Z}) \\ &\times (\tilde{x} - \tilde{y}) \tilde{F}(\tilde{x}, \tilde{y}, \tilde{z}) \tilde{Y}(\tilde{Y}^2 - \tilde{Z}^2) \mathcal{W}(\tilde{y}, \tilde{z}, \tilde{Y}, \tilde{Z}) \\ &\times e^{-\frac{1}{2}(15\tilde{y}^2+5\tilde{z}^2)} e^{-\frac{1}{2}(15\tilde{Y}^2+5\tilde{Z}^2)} e^{-\frac{1}{2}\tilde{x}^2(1-\gamma^2)} \\ &\times e^{-\frac{1}{2}(\tilde{\nu}+\tilde{Y}-\gamma\tilde{x})^2} p(\ln m|\mathbf{X}), \quad (\text{A8}) \end{aligned}$$

where $N \equiv 5^5 3^4 / (2\pi)^2$, $\{\tilde{x}, \tilde{y}, \tilde{z}\} = \{x, y, z\} / \sqrt{1-\gamma^2}$, $\{\tilde{\nu}, \tilde{Y}, \tilde{Z}\} = \{\delta_c, Y, Z\} / (\sigma_0 \sqrt{1-\gamma^2})$, $\tilde{F}(\tilde{x}, \tilde{y}, \tilde{z}) = \tilde{y}(\tilde{y}^2 - \tilde{z}^2)(\tilde{x} - 2\tilde{z})((\tilde{x} + \tilde{z})^2 - 9\tilde{y}^2)$, the function $\chi(s, t, u)$ is unity when $-t \leq u \leq t$, $t \geq 0$, $s \geq 3t - u$ and is zero otherwise, and the function $\mathcal{W}(\tilde{y}, \tilde{z}, \tilde{Y}, \tilde{Z})$ which captures the effect of marginalising over the relative Euler angles has the Taylor expansion (Desjacques 2008)

$$\begin{aligned} \mathcal{W}(\tilde{y}, \tilde{z}, \tilde{Y}, \tilde{Z}) &= 1 + \frac{\kappa^2}{10} \mathcal{W}_2 + \frac{\kappa^3}{105} \mathcal{W}_3 + \frac{\kappa^4}{280} (\mathcal{W}_2)^2 \\ &+ \frac{\kappa^5}{2310} \mathcal{W}_2 \mathcal{W}_3 + \mathcal{O}(\kappa^6), \quad (\text{A9}) \end{aligned}$$

where $\kappa \equiv 5\gamma/4$ and

$$\begin{aligned} \mathcal{W}_2 &= 16 (3\tilde{y}^2 + \tilde{z}^2) (3\tilde{Y}^2 + \tilde{Z}^2), \\ \mathcal{W}_3 &= 64\tilde{z}\tilde{Z} (9\tilde{y}^2 - \tilde{z}^2) (9\tilde{Y}^2 - \tilde{Z}^2). \quad (\text{A10}) \end{aligned}$$

The integrals over \tilde{y} , \tilde{z} and \tilde{Z} are tedious but can be expressed in closed form. The remaining integrals over \tilde{x} , \tilde{Y} and σ_0 must be done numerically. Figure A1 shows the result of the zeroth order calculation and that of successively including higher powers of κ , with standard mass assignment. We see that the odd powers do not contribute significantly. The even powers, however, have not converged since the κ^4 term gives a significant contribution compared to the second order calculation. Presumably one would have to continue the calculation at least to order κ^6 (if not κ^8), to get reasonable convergence.

A3 A simpler way out

As the results of the previous section show, it rapidly becomes very complicated to deal with the full stochasticity inherent in even a simple barrier prescription like equation (28). Luckily, approximating this barrier with the deterministic expression (33) leads to an excellent description of the mass function of ESPEaks found using the stochastic barrier (28) (compare the dashed black curve in Figure 1 with the solid orange histogram.)

The calculation proceeds by setting $B = \delta_c + 0.5\sigma_0$ and $\dot{B} = 0.5$ in equation (A4), which means that the excursion set constraint is independent of Y and Z . These variables, together with the problematic relative Euler angles between the tensors, can then be trivially marginalised over, without having to Taylor expand as in equation (A9). The remaining variables can then be dealt with exactly like in BBKS; the only integral that cannot be done analytically is the one over x ,

since this involves the BBKS curvature function $F(x)$ given by

$$F(x) = \frac{1}{2} (x^3 - 3x) \left\{ \operatorname{erf} \left(x \sqrt{\frac{5}{2}} \right) + \operatorname{erf} \left(x \sqrt{\frac{5}{8}} \right) \right\} + \sqrt{\frac{2}{5\pi}} \left[\left(\frac{31x^2}{4} + \frac{8}{5} \right) e^{-5x^2/8} + \left(\frac{x^2}{2} - \frac{8}{5} \right) e^{-5x^2/2} \right], \quad (\text{A11})$$

(equations A14–A19 in BBKS). This is, of course, exactly the calculation performed by Paranjape & Sheth (2012) and later used by Paranjape et al. (2013).

The main message here is that the barrier stochasticity induced by ellipsoidal effects is a technical detail that does not address the main problem – that of mass re-assignment – we are faced with. Rather, the simplicity of the deterministic barrier solution allows us to tackle this problem in a computationally straightforward way, as discussed in the main text. In principle, one could imagine having a physically better motivated model of mass re-assignment; provided it can be expressed in the formal language of equation (37), the hurdles in using it to make mass function predictions would be purely technical.

APPENDIX B: ELLIPSOIDAL DYNAMICS AND COLLAPSE-TIME UNCERTAINTY

To understand why one might expect a small systematic uncertainty in the predicted collapse time in ellipsoidal dynamics, it will help to first recapitulate some of the basic features of *spherical* collapse.

Consider the simplest case of an Einstein-deSitter (EdS; $\Omega_{\text{tot}} = \Omega_{\text{m}} = 1$) background. Recall that the comoving Eulerian radius R and overdensity $\Delta = \rho/\bar{\rho}$ of a collapsing homogeneous sphere with initial overdensity $\delta_i = (5/3)\delta_0/(1+z_i) > 0$ and comoving Lagrangian radius R_0 are given by (Gunn & Gott 1972)

$$\Delta = (R_0/R)^3 = \frac{9(\theta - \sin \theta)^2}{2(1 - \cos \theta)^3}, \quad \frac{\delta_0}{1+z} = \delta_0 \left(\frac{t}{t_0} \right)^{2/3} = \delta_{\text{L}} = \frac{3}{5} \left(\frac{3}{4} \right)^{2/3} (\theta - \sin \theta)^{2/3}, \quad (\text{B1})$$

where t_0 is the present epoch and δ_{L} is the linear overdensity extrapolated to redshift z . The radius turns around at $\theta = \pi$ and reaches zero at $\theta = 2\pi$. In the standard approach, instead of evolving the solution to zero radius, one argues that the radius will become essentially constant once the object virializes. While this is not captured by the spherical model, a simple energy conservation argument says that the physical “virial radius” must be one half of the physical radius at turn-around.

The key conceptual point here is that the model itself reaches the virial radius at $t_{\text{vir}} = t(\theta = 3\pi/2)$ which occurs slightly before the collapse-time $t_{\text{coll}} = t(\theta = 2\pi)$; in particular, $t_{\text{vir}} \approx 0.91 \times t_{\text{coll}}$. However, one can argue that virialization actually occurs over a dynamical timescale t_{dyn} (the free-fall time at virialization; see, e.g., Padmanabhan 1993) which, coincidentally, is of order 10% of the collapse time. So in practice it is quite reasonable to use $t_{\text{coll}} (\approx t_{\text{vir}} + t_{\text{dyn}})$ in place of t_{vir} when computing the linearly extrapolated overdensity, which gives the well-known result $\delta_{\text{L}} = 1.686$. (Had we instead evaluated δ_{L} at $\theta = \theta_{\text{vir}}$, we would get $\delta_{\text{L}} = 1.583$, a $\sim 6\%$ decrement from the traditional value; see, e.g., Bond & Myers 1996, hereafter, BM96).

The nonlinear overdensity at virialization follows from energy conservation and matching to the turn-around time t_{ta} :

$$\begin{aligned} \Delta_{\text{vir}} &= \Delta_{\text{ta}} (t_{\text{vir}}/t_{\text{ta}})^2 (R_{\text{phys,ta}}/R_{\text{phys,vir}})^3 \\ &= (9\pi^2/2) (t_{\text{vir}}/t_{\text{ta}})^2 \\ &\approx (9\pi^2/2) (t_{\text{coll}}/t_{\text{ta}})^2 = 18\pi^2. \end{aligned} \quad (\text{B2})$$

Notice that the traditional value of $18\pi^2 \simeq 178$ arises after approximating $t_{\text{vir}} \approx t_{\text{coll}}$; the actual nonlinear density at t_{vir} would be $\sim 20\%$ smaller.

In the ellipsoidal model discussed by BM96 (see also White & Silk 1979; Eisenstein & Loeb 1995; Monaco 1999), it is more difficult to identify conserved quantities since there is no spherical symmetry and nonlinear tides can have a complicated influence. The definition of virialization is therefore somewhat ambiguous. BM96 settled on a simple prescription in which each principle axis is evolved nonlinearly until it shrinks to a predetermined fraction f_c of the global scale factor, after which it is assumed to remain fixed at that value. Collapse is defined as the time at which the longest axis (i.e., the smallest shear eigenvalue) satisfies this condition. Choosing $f_c = 0.178$ ensures that the overdensity at virialization for a spherical configuration is $f_c^{-1/3} \simeq 178$, the traditional value. Since there is no compensation for dynamical timescales, it seems reasonable that this prescription *underpredicts* collapse times. In the spherical limit, this would be a $\sim 10\%$ effect as discussed above.

The fit (29) by Sheth et al. (2001) to the resulting linear overdensity values at collapse as a function of ellipticity and prolateness reduces to the traditional spherical collapse result when $Z = 0 = Y$, meaning that it rescales the BM96 prescription for the barrier by a factor $1.686/1.583 = 1.06$. This would cause a corresponding $\sim 10\%$ increase in collapse time. While this increase is of the correct magnitude in the spherical limit (see above), it is less clear whether this is also true for significantly triaxial configurations. In the EdS case where the growth factor is proportional to the scale factor, one can check that a barrier-rescaling as above does, in fact, rescale the collapse time by a constant at any ellipticity. However, the situation is different, e.g., in flat Λ CDM with $\Omega_{\text{m}} < 1$. In this case, the growth factor is different from the scale factor and one can show that a barrier-rescaling leads to a slightly *larger* effect on the collapse time for $e_{\text{v}} > 0$ than it does for $e_{\text{v}} = 0$. In other words, if one were aiming for a $\sim 10\%$ increase in collapse time for all ellipticities, then rescaling the barrier by a constant will tend to overcompensate at large ellipticities, and would go in the direction of explaining the results of Section 5.3.

Of course, the specific prescription for virialization itself is somewhat ad-hoc, and BM96 discuss several modifications, all of which lead to few percent changes in collapse time (see also Angrick & Bartelmann 2010; Ludlow & Porciani 2011a). Additionally, the specific choice of halo finder in the simulation will also lead to (probably unquantifiable) systematics. It is therefore not unreasonable that uncertainties in dynamical modelling lead to a small (but, in the WDM case, important) systematic overprediction of collapse times.

APPENDIX C: PEAK SHAPES AND THE COLLAPSE THRESHOLD

Figure C1 shows the distributions of ellipticity and prolateness defined using the tidal tensor (top panel) and using the Hessian of the density (bottom panel), coloured by the halo mass in

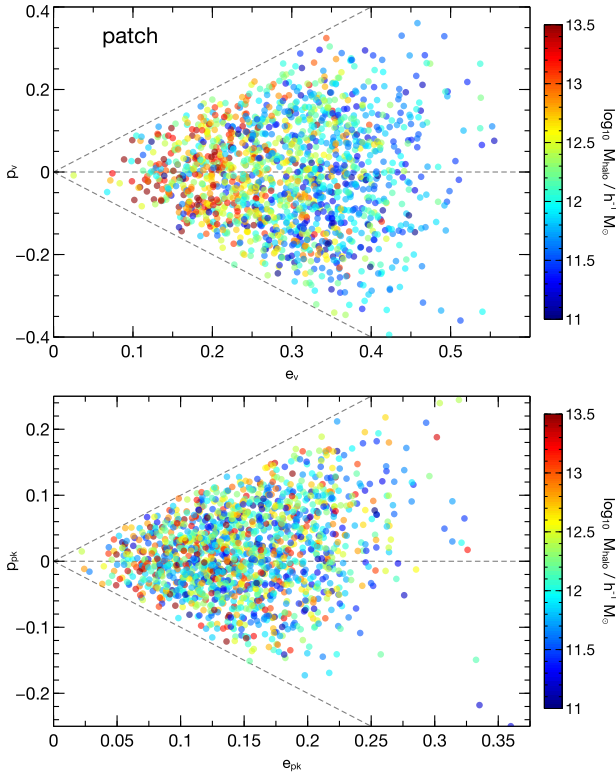


Figure C1. (*Top panel:*) The distribution of patch-averaged ellipticity e_v (equation 17) and prolateness p_v (equation 18) of the tidal tensor $\partial_{ij}\psi$, coloured by halo mass. Both the median value and scatter of e_v increases with decreasing halo mass, whereas we find no trend in p_v with halo mass. (*Bottom panel:*) Corresponding patch-averaged quantities e_{pk} (equation 19) and p_{pk} (equation 20) defined for the density Hessian $\partial_{ij}\delta$. (Note that the scale on the axes is different from the top panel.) There is a weak preference for low mass objects to have $p_{pk} > 0$, which is consistent with the BBKS results for peak shapes.

each case. These quantities were defined in equations (17)-(20) above.

In the top panel we see that low mass haloes have a weak preference for larger values of ellipticity e_v , while there is no trend of prolateness p_v with mass. This is consistent with the results of Ludlow & Porciani (2011b) and Despali et al. (2013) for CDM haloes. In the bottom panel (note the difference in axes scales) we see that there is a large scatter in values of e_{pk} at any mass, while there is a weak trend for $p_{pk} > 0$ at low masses. The latter is consistent with the BBKS results for peak shapes.

We noted earlier that the barrier (29) associated with ellipsoidal dynamics does not describe the measured densities of the proto-halo patches; in particular, we found no correlation between the measured proto-halo density and prolateness. We have repeated the exercise of finding ES Peaks and matching them with proto-haloes using the full ellipsoidal collapse barrier (29). While we find that a similar fraction ($\sim 62\%$) of proto-haloes have matching ES Peaks, the scatter in the assigned masses, especially at low masses, is somewhat larger in this case as compared to using equation (28). Figure C2 compares the mass distributions of matched objects in these two cases.

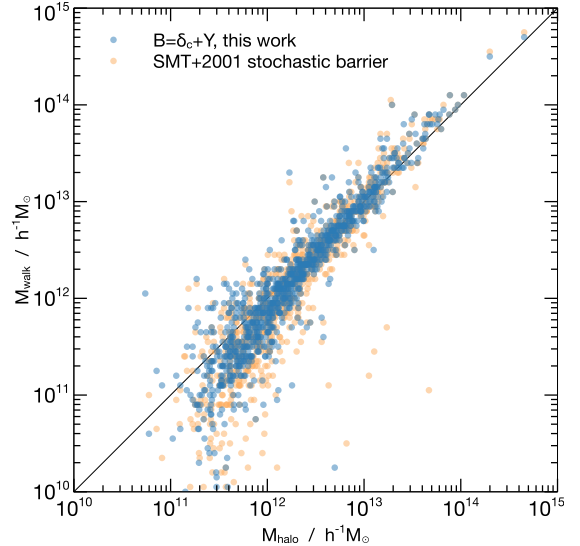


Figure C2. Comparing ES Peak masses assigned by the algorithm described in Section 4.1 when using the simple stochastic barrier (equation 28; blue points) and when using the fully stochastic SMT01 barrier (equation 29; orange points). The points show the masses M_{halo} of proto-haloes that could be matched to ES Peaks, against ES Peak mass M_{walks} . In both cases the matched fraction was comparable (64% when using equation 28 and 62% when using equation 29); however, the scatter when using the SMT01 barrier is somewhat larger than when using equation (28), especially at low masses, which can be traced to the fact that the SMT01 barrier introduces a dependence of the peak-centred overdensity on prolateness which is not present in the case of the actual proto-haloes.